## **OPEN ACCESS**



## The Comprehensive Archive of Substellar and Planetary Accretion Rates

S. K. Betti<sup>1</sup>, K. B. Follette<sup>2</sup>, K. Ward-Duong<sup>3</sup>, A. E. Peck<sup>3,4</sup>, Y. Aoyama<sup>5</sup>, J. Bary<sup>6</sup>, B. Dacus<sup>2,7</sup>, S. Edwards<sup>3</sup>, G.-D. Marleau<sup>8,9,10,11</sup>, K. Mohamed<sup>2,12</sup>, J. Palmo<sup>2,13</sup>, C. Plunkett<sup>2</sup>, C. Robinson<sup>2</sup>, and H. Wang<sup>2</sup>

Department of Astronomy, University of Massachusetts, Amherst, MA 01003, USA; sbetti@stsci.edu

Department of Physics and Astronomy, Amherst College, Amherst, MA 01003, USA

Department of Astronomy, Smith College, Northampton, MA 01063, USA

Department of Astronomy, New Mexico State University, Las Cruces, NM 88003, USA

Kavli Institute for Astronomy and Astrophysics, Peking University, Beijing 100871, People's Republic of China

Department of Physics and Astronomy, Colgate University, Hamilton, NY 13346, USA

Department of Astronomy and Astrophysics, University of California, San Diego, La Jolla, CA 92093, USA

Brakultät für Physik, Universität Duisburg-Essen, Lotharstraße 1, D-47057 Duisburg, Germany

Institut für Astronomie und Astrophysik, Universität Tübingen, Auf der Morgenstelle 10, D-72076 Tübingen, Germany

Institut für Astronomie, Königstuhl 17, D-69117 Heidelberg, Germany

Physikalisches Institut, Universität Bern, Gesellschaftsstr. 6, 3012 Bern, Switzerland

Max-Planck-Institut für Astronomie, Königstuhl 17, D-69117 Heidelberg, Germany

Department of Civil and Environmental Engineering, Massachusetts Institute of Technology, Cambridge, MA 02139, USA

Received 2023 May 26; revised 2023 September 19; accepted 2023 September 28; published 2023 November 23

#### **Abstract**

Accretion rates  $(\dot{M})$  of young stars show a strong correlation with object mass (M); however, extension of the  $\dot{M}-M$  relation into the substellar regime is less certain. Here, we present the Comprehensive Archive of Substellar and Planetary Accretion Rates (CASPAR), the largest compilation to date of substellar accretion diagnostics. CASPAR includes: 658 stars, 130 brown dwarfs, and 10 bound planetary mass companions. In this work, we investigate the contribution of methodological systematics to scatter in the  $\dot{M}-M$  relation and compare brown dwarfs to stars. In our analysis, we rederive all quantities using self-consistent models, distances, and empirical line flux to accretion luminosity scaling relations to reduce methodological systematics. This treatment decreases the original  $1\sigma$  scatter in the  $\log \dot{M} - \log M$  relation by  $\sim 17\%$ , suggesting that it makes only a small contribution to the dispersion. The CASPAR rederived values are best fit by  $\dot{M} \propto M^{2.02\pm0.06}$  from  $10\,M_{\rm J}$  to  $2\,M_{\odot}$ , confirming previous results. However, we argue that the brown-dwarf and stellar populations are better described separately and by accounting for both mass and age. Therefore, we derive separate age-dependent  $\dot{M}-M$  relations for these regions and find a steepening in the brown-dwarf  $\dot{M}-M$  slope with age. Within this mass regime, the scatter decreases from 1.36 dex to 0.94 dex, a change of  $\sim 44\%$ . This result highlights the significant role that evolution plays in the overall spread of accretion rates, and suggests that brown dwarfs evolve faster than stars, potentially as a result of different accretion mechanisms.

Unified Astronomy Thesaurus concepts: Brown dwarfs (185); Stellar accretion (1578); Classical T Tauri stars (252); Astronomy databases (83); Pre-main sequence stars (1290)

Supporting material: machine-readable table

#### 1. Introduction

In the classical picture of star formation, molecular cloud cores collapse under gravity to form new stars. As the cores collapse, rotational velocity and conservation of angular momentum causes infalling material to settle into a circumstellar disk (Hartmann 1998). These primordial disks have been found to have a lifetime of ~1–10 Myr (e.g., Strom et al. 1989; Armitage et al. 2003; Sicilia Aguilar et al. 2006; Li & Xiao 2016), during which time they provide the material essential for both planet formation (Mamajek 2009) and stellar accretion (Hartmann et al. 2016). The evolution and dispersal of the disk unfold through several processes. Planet formation occurs through core accretion of planetesimals in the inner few astronomical units (Safronov & Zvjagina 1969; Hayashi et al. 1985; Pollack et al. 1996), leading to terrestrial planet formation, while in the outer disk, core accretion,

Original content from this work may be used under the terms of the Creative Commons Attribution 4.0 licence. Any further distribution of this work must maintain attribution to the author(s) and the title of the work, journal citation and DOI.

fragmentation, and instabilities are theorized to form giant gaseous protoplanets (Kuiper 1951; Cameron 1978; Boss 1997; Bate et al. 2002, 2003; Johnson & Gammie 2003; Rafikov 2005; Cai et al. 2006). Through the T Tauri phase, the disks are also actively accreting material onto the star, enabled by a combination of viscous accretion through the magnetorotational instability (Hawley & Balbus 1991) and/or MHD disk winds, depending on the physical conditions in the disk (Lesur et al. 2023; Pascucci et al. 2023). Additionally, strong near-UV, far-UV, and/or X-ray radiation from the star and its accretion shock can heat the gaseous disk surface, leading to thermally driven photoevaporative winds beyond the gravitational radius, which likely account for the final clearing of the disk gas (Alexander et al. 2014 and references therein).

Within a few stellar radii of the star (traditionally assumed to be  $\sim 5 R_{\odot}$ ; Gullbring et al. 1998), the disk is interrupted by strong stellar magnetic fields and disk material flows to the stellar surface along accretion columns following magnetic field lines, resulting in strong shocks on the stellar surface. The resultant emission from the accretion onto the star includes broad emission lines in the free-falling magnetospheric flows

(Muzerolle et al. 2001; Hartmann et al. 2016), though Dupree et al. (2014) suggested that in the case of hydrogen, the broad lines could be formed in a turbulent postshock region and forbidden lines from accretion shocks and winds (Hartigan et al. 1995). When the gas shocks on the stellar photosphere, the already fully ionized gas heats to 10<sup>6</sup> K. The optically thin preshock region is seen primarily as Balmer continuum excess (Valenti et al. 1993; Calvet & Gullbring 1998; Gullbring et al. 1998, 2000), while the optically thick postshock region emits Paschen continuum excess<sup>14</sup> (Calvet & Gullbring 1998). These sources of excess continuum emission result in the veiling of photospheric absorption lines. Accretion rates measured from both optically thin and thick shock regions can be inferred from the total excess luminosity produced by accretion; however, there is currently no direct method to measure the mass accretion rate (M) from the emission produced in the accretion flows. Instead, a scaling relation must be applied to relate a single emission-line luminosity to a mass accretion rate.

Comprehensive multiwavelength studies have found that  $\dot{M}$  decreases with decreasing stellar mass (M; Muzerolle et al. 2003; Calvet et al. 2004; Herczeg & Hillenbrand 2008; Alcalá et al. 2014; Manara et al. 2017b), following a power law of  $\dot{M} \propto M^2$  in the stellar regime. This mass accretion rate—mass ( $\dot{M}-M$ ) relation has been assumed to extend from the stellar to the substellar ( $M \leqslant 0.075 M_{\odot}$ ) regime with no variation in slope (e.g., Muzerolle et al. 2003, 2005; Mohanty et al. 2005), though some studies suggest a break to a steeper relation around 0.2  $M_{\odot}$  for older star-forming regions (SFRs; Manara et al. 2017a; Alcalá et al. 2017). Additionally, at all masses, there is significant 1–2 dex scatter in accretion rates. Within the stellar regime, Manara et al. (2023) assert that the majority of this scatter results from physical variation and not observational uncertainty.

Various studies have looked at possible physical mechanisms responsible for this dispersion in the  $\dot{M}$ -M relation. These include: intrinsic variability and the decrease of  $\dot{M}$  with age (e.g., Natta et al. 2006; Costigan et al. 2014; Venuti et al. 2014; Hartmann et al. 2016), differences in the properties of star-forming cores (e.g., Clarke & Pringle 2006; Dullemond et al. 2006; Ercolano et al. 2014), competition among accretion mechanisms (viscosity or gravitational instability; e.g., Vorobyov & Basu 2008, 2009; DeSouza & Basu 2017), multiplicity (e.g., Zagaria et al. 2022), and, for planetary mass companions (PMCs), differences in the instability threshold and reservoir for accretion as a result of disk fragmentation (e.g., Stamatellos & Herczeg 2015). However, systematic studies of large numbers of accreting substellar objects are lacking, and it is not clear if this proposed explanation holds in this low-mass regime.

Additionally, scaling relationships between line emission and accretion luminosity have been empirically developed and calibrated for stars for a wide variety of emission lines (Natta et al. 2004; Rigliaco et al. 2011; Alcalá et al. 2014, 2017). It is not clear to what extent empirical scaling relations are valid in the substellar regime, where potential differences in accretion (magnetospheric and planetary shock) and physical parameters (energy loss, magnetic field strength, temperature of accreting gas, gravitational potential, and disk mass), could alter the

relationship between line luminosity and the mass accretion rate (Thanathibodee et al. 2019; Aoyama et al. 2020). In order to understand the origin and accretion of both bound PMCs (which include protoplanet candidates, e.g., PDS 70b and c, Delorme 1 (AB)b, and LkCa 15b; Sallum et al. 2015; Wagner et al. 2018; Haffert et al. 2019; Eriksson et al. 2020; Betti et al. 2022; Ringqvist et al. 2023) and brown-dwarf (BD) companions, objects in bound orbits around a higher-mass host (which we define as bound objects below  $M < 30\,M_{\rm J}$ ; see Martinez & Kraus 2019)), and young BDs (hereafter, all considered substellar objects), we first must characterize the physical (e.g., variability and age) and systematic (e.g., accretion-rate tracer and evolutionary model) properties that affect accretion-rate estimates.

The aim of this paper is threefold: (a) to provide the largest compilation to date of BD and protoplanet accretion rates derived under a uniform methodology; (b) to investigate methodological differences in the scatter of the  $\dot{M}$ -M relation between stars and BDs; and (c) to determine whether the statistics of  $\dot{M}$  measurements suggest accretion differences between these mass populations. In Section 2, we give an overview of the Comprehensive Archive of Substellar and Planetary Accretion Rates (CASPAR). In Section 3, we rederive object properties (e.g., mass, distance, and temperature) in a consistent manner. In Section 4, we detail the technique we applied to derive linear fits for the  $\dot{M}$ -M relation. We also present an updated  $\dot{M}$ -M relation and discuss the role of methodology in producing scatter in Section 5. In Section 6, we quantify the contribution of various drivers producing the physical scatter observed in the overall  $\dot{M}$ -M relation, and in Section 7, we focus on the BD population. In Section 8, we discuss how these phenomena affect our interpretation of accretion in the substellar regime. The results are then summarized in Section 9.

## 2. Overview of the Database

We have assembled accretion rates for young PMCs, BDs, and Classical T Tauri stars (CTTSs) from large surveys of accreting objects, as well as individual object papers. This database consists of two parts: a compilation of published accretion properties, unmodified from their source publications (hereafter, the Literature Database), and a unified rederivation of accretion properties from these studies, CASPAR. <sup>15</sup>

We have focused on collecting properties for known accreting substellar objects. Within the Literature Database, 86 objects are considered substellar (below the hydrogenburning limit, or HBL,  $M < 0.075 M_{\odot}$ ; e.g., Mohanty et al. 2005), of which 10 are PMCs (five are protoplanets and five are  $M < 30 M_{\rm I}$  BDs). The database also includes a substantial compilation of CTTS accretion rates for stars later than G spectral type. We exclude Herbig stars, as detailed accretion census papers for this population already exist (e.g., Guzmán-Díaz et al. 2021; Vioque et al. 2022) and we are particularly focused on substellar accretion. To date, we have compiled data for 798 objects from 46 studies, for a total of 1058 independent accretion measurements spanning 24 yr, from 1998 to early 2022. The list of references is given in Table 1. The sky positions for all objects are shown in Figure 1. As many of the objects are in associations and clusters with small angular

<sup>&</sup>lt;sup>14</sup> In the NIR, excess continuum emission from dust is also produced at the inner edge of the disk, due to heating by radiation from the photosphere and shocked regions (Johns-Krull & Valenti 2001; Muzerolle et al. 2003; Fischer et al. 2011).

<sup>15</sup> CASPAR is openly available on Zenodo: https://doi.org/10.5281/zenodo.

**Table 1**Literature Reference SFRs

References	SFR	# Objects
Alcalá et al. (2014)	Lupus	36
Alcalá et al. (2017)	Lupus	43
Alcalá et al. (2019)	Lupus 4	1
Alcalá et al. (2020)	Lupus	1
Alcalá et al. (2021)	Taurus–Auriga	5
Betti et al. (2022)	Tucana-Horologium	1
Bowler et al. (2011)	Upper Scorpius	1
Calvet & Gullbring (1998),	Taurus	17
Gullbring et al. (1998)		
Close et al. (2014)	Sco OB2-2	1
Comerón et al. (2010)	$\rho$ Ophiuchus	1
Eriksson et al. (2020)	Tucana-Horologium	1
Espaillat et al. (2008)	25 Orionis	1
Gatti et al. (2006)	$\rho$ Ophiuchus	16
Gatti et al. (2008)	$\sigma$ Orionis	35
Haffert et al. (2019)	Centaurus	2
Hashimoto et al. (2020)	Centaurus	2
Herczeg & Hillenbrand (2008)	Taurus, TW HyA	24
Herczeg et al. (2009)	Upper Scorpius, TW HyA Taurus, Chamaeleon I	12
Ingleby et al. (2013)	*	19
Kalari & Vink (2015) Kalari et al. (2015)	Sh 2-284 Lagoon Nebula	3 225
Lee et al. (2020)	Argus	1
Manara et al. (2015)	$\rho$ Ophiuchus	17
Manara et al. (2016a)	ρ Opiniuciius Chamaeleon I	38
Manara et al. (2017b)	Chamaeleon I	49
Manara et al. (2020)	Upper Scorpius	35
Manara et al. (2021)	Orion OB1	11
Mohanty et al. (2005)	Chamaeleon I, IC348,	22
Monanty et al. (2003)	Taurus	
Muzerolle et al. (2003)	Taurus, IC348	13
Muzerolle et al. (2005)	Taurus, Chamaeleon I	33
Natta et al. (2004)	Chamaeleon I, ρ Ophiuchus	19
Natta et al. (2006)	$\rho$ Ophiuchus	112
Nguyen-Thanh et al. (2020)	Upper Scorpius	1
Petrus et al. (2020)	Upper Scorpius	7
Pouilly et al. (2020)	Taurus	1
Rigliaco et al. (2011)	$\sigma$ Orionis	63
Rigliaco et al. (2012)	$\sigma$ Orionis	8
Rugel et al. (2018)	$\eta$ Chamaeleontis	15
Sallum et al. (2015)		1
Salyk et al. (2013)	Taurus, Upper Centaurus Lupus,	35
	$\rho$ Ophiuchus, Upper Scorpius,	
	Lupus, Chamaeleon I	
Santamaría-Miranda et al. (2018)	$\rho$ Ophiuchus	1
Venuti et al. (2019)	TW Hydrae	9
Wagner et al. (2018)	Upper Centaurus Lupus	1
White & Basri (2003)	Taurus-Auriga	10
Wu et al. (2015)	Chamaeleon I	1
Wu et al. (2017)	Lupus	1
Zhou et al. (2014)	Taurus, Lupus, Upper Scorpius	3

scales, they appear as a single point. We show zoomed-in views of six of the regions as insets.

As this sample is compiled from many individual studies, it is an incomplete survey of nearby objects in both mass and volume. In Figure 2, we show the mass function of our sample with uniformly rederived masses (as discussed in Section 3),

colored by age and compared to the Chabrier (2005) initial mass function (IMF) and Kirkpatrick et al. (2021) field BD mass function, all normalized so the integral over mass is 1. The mass distribution of objects in CASPAR is consistent with the IMF, though there is a difference at  $0.1-0.3\,M_\odot$ , likely due to the undersampling of objects at all ages in this mass range. A majority of the CASPAR objects are young (<3 Myr), as expected, since disk fraction rapidly declines after 2.5–3 Myr (Mamajek 2009).

From the Chabrier (2005) IMF, if all of the SFRs follow the same IMF, we would expect ~20% more substellar objects. These missing objects have either (a) not been surveyed or (b) were initially missed when compiling CASPAR. For example, when we compare CASPAR objects in  $\rho$  Ophiuchus to the census from Esplin & Luhman (2020; complete up to spectral types earlier than M6), we find (as shown in Figure 3) that CASPAR includes 86% of all known  $\rho$  Ophiuchus substellar objects (32 of 37;  $M < 0.075 \, M_{\odot}$ ;  $\leq$  M5.5) with optically thick disks (which we use as a proxy for potential to be accreting).

The broad classes of object properties included in the database are summarized in Table 2, with individual column headers listed in Appendix A. Both the Literature Database and CASPAR have identical columns. Each accretion rate is assigned its own row and a unique number identifier, identical between the two databases. Therefore, an object observed at multiple epochs has multiple unique number identifiers. Each object is also identified with a unique name. Mass accretion rates have been measured from four broad accretion diagnostics families, namely: continuum excess, line luminosity,  $H\alpha$  photometric luminosity, and line profile. In Appendix B, we discuss in more detail the process of compiling the Literature Database and the kinematic, photometric, and age information for each object.

We show all literature database accretion rates as a function of mass colored by their accretion diagnostic in Figure 4. Overall, we see that the accretion rates vary by 2 orders of magnitude while still following an empirical power-law relationship between accretion rate and mass,  $\dot{M} \propto M^{2.15}$  (black line), similar to other empirically derived relations (Muzerolle et al. 2003, 2005; Mohanty et al. 2005; Alcalá et al. 2017). However, as shown in the bottom panel of Figure 4, we do find systematic offsets and variable slopes in the  $\dot{M} \propto M^x$  relation when we fit by accretion diagnostic (see Section 4 for the fit details), which will be discussed in Section 5.2.

## 3. Unified Derivation of Quantities

The studies in the literature compilation come from a variety of instruments, analysis pipelines, and accretion tracers, which likely contribute to the wide dispersion of accretion rates at a single mass (i.e., the scatter). Additionally, the dependence of the mass and radius estimates on the application of a variety of different evolutionary models and spectral fitting tools also introduces scatter (see the gray dashed lines in the top panel of Figure 4). In order to remove these effects, we first investigate the dispersion introduced by methodology by re-estimating the object and accretion parameters under a unified set of assumptions and by comparing them to Literature Database values. Estimates of PMC spectral types and masses are highly uncertain and have been estimated from a variety of methods, including kinematics, orbital fitting, and spectral fitting. Due to the larger uncertainties in deriving accurate masses for the lowest-mass objects, we focus here only on stars and BDs.

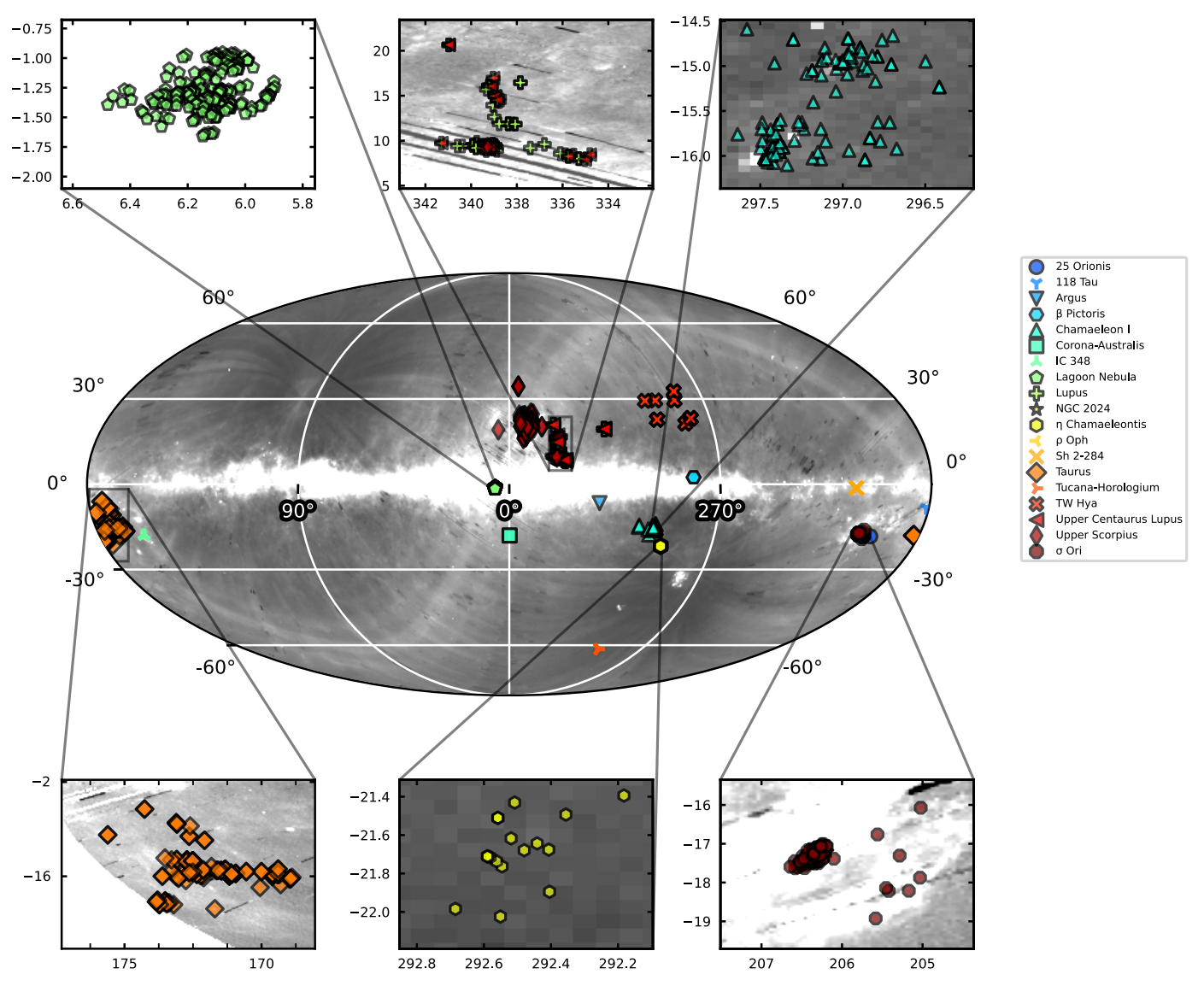


Figure 1. All-sky map indicating all objects in CASPAR colored by SFR or association overlaid on a 65  $\mu$ m all-sky map (Doi et al. 2015; Takita et al. 2015). Insets: enlarged views of several nearby SFRs.

Updating the PMC entries so that their masses are uniform and comparable to the full CASPAR sample will be the subject of future work. As a result, in the remainder of this study, we use the Literature Database mass and accretion-rate estimates for PMCs in our plots and calculations. While we fit this PMC population and report it here, we do not attempt to infer any trends, as these accretion rates and masses are not rederived under a unified system.

In this work, we update and unify literature values by performing the following modifications:

- 1. adopt Gaia Data Release 2 (DR2)/Early Data Release 3 (EDR3; Gaia Collaboration et al. 2018, 2021) distances when available (*N* = 604; Bailer-Jones et al. 2018, 2021);
- 2. adopt single ages for each SFR (or subregion, where available);
- 3. adopt the spectral type-temperature conversion from Herczeg & Hillenbrand (2014);
- 4. extract mass, luminosity, radius, and surface gravity using the MIST MESA models (Paxton et al. 2011, 2013, 2015; Choi et al. 2016; Dotter 2016), K

spectral types, and Baraffe et al. (2015) evolutionary models for all others;

- 5. calculate accretion luminosities using the Alcalá et al. (2017)  $L_{\rm acc}$ – $L_{\rm line}$  scaling relationships—for excess-continuum-based accretion luminosity estimates, we scale by  $d^2$  from Gaia DR2/EDR3; and
- 6. from the accretion luminosity, we calculate the mass accretion rate as

$$\dot{M} = \left(1 - \frac{R}{R_{\rm in}}\right)^{-1} \frac{L_{\rm acc}R}{GM},\tag{1}$$

where  $\dot{M}$  is the mass accretion rate, R is the stellar radius,  $R_{\rm in}$  is the truncation radius, which we assume to be  $5\,R_{\odot}$  (Gullbring et al. 1998), M is the stellar mass, G is the gravitational constant, and  $L_{\rm acc}$  is the accretion luminosity.

We describe the unified methodology for deriving each parameter in full detail in Appendix C.

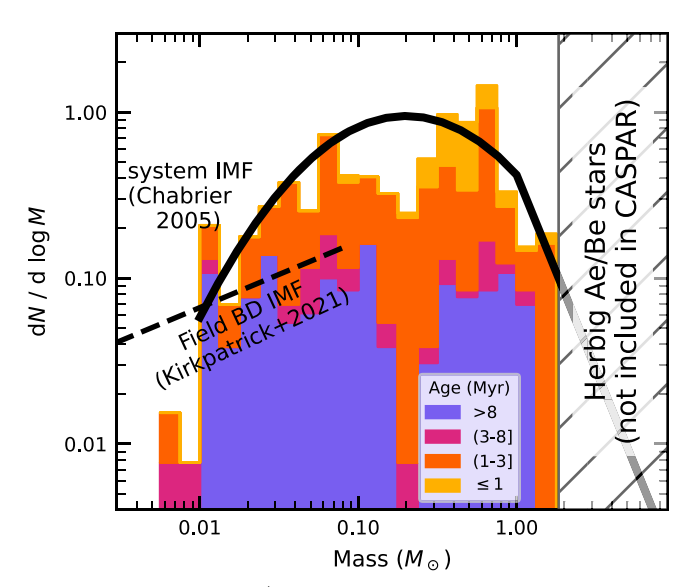
We show comparisons of the rederived CASPAR parameters and the literature parameters in Figure 5. For all rederived quantities, 50%–89% are within a factor of 2 of the literature

Table 2
CASPAR Sections<sup>a</sup>

Section	Description
ID Information	Source and literature reference IDs
Flags	Duplication, binary, and companion flags
Kinematic, Photometry, and Age	6D Gaia kinematics, NIR photometry, and age/associations
Reference and Physical Parameters	Literature observations information and stellar information
Emission Lines	Individual emission-line flux and accretion rates
Accretion Rates	Final accretion luminosity and accretion rates
Model and Scaling References	References for spectral type/temperature conversions, evolutionary models, and scaling relations

#### Note.

<sup>&</sup>lt;sup>a</sup> See Table 6 for descriptions of individual columns.



**Figure 2.** Mass function  $(dN/d \log M)$  of the 793 objects in CASPAR colored by stellar age (stacked histogram). The IMF for multiple systems from Chabrier (2005) and the field BD IMF from Kirkpatrick et al. (2021) are shown for comparison. Herbig Ae/Be stars are purposely excluded from CASPAR, as we are primarily focused on substellar objects.

value, indicative of the relatively small effects of these updates. The change from individual or previous estimates of SFR ages to a uniform set of ages results in the large dispersion seen between the original and rederived values.

We find that 60 objects that were originally considered lowmass stars with masses  $> 0.075 M_{\odot}$  are now classified as BDs with masses below the HBL (conversely, six of the BDs are now classified as stars). We highlight these in the lower right quadrant of Figure 5. Of those,  $\sim$ 20 are within  $1\sigma$  of the HBL. These mass shifts result from using the Herczeg & Hillenbrand (2014) spectral type-to-temperature conversion and updated ages that were not used by the original references. Of the 16 studies where objects traverse below the HBL, 11 were published before the Herczeg & Hillenbrand (2014) spectral type-temperature conversion; therefore, their methods of calculating temperature and spectral types differed (with the majority using the conversion of Luhman et al. 2003), leading to differences when reevaluating them. The four published after Herczeg & Hillenbrand (2014) utilized their own spectral fitting and used the spectral type-temperature conversion of Luhman et al. (2003) for the M dwarfs in their sample. When we look at the temperature-spectral type conversions from

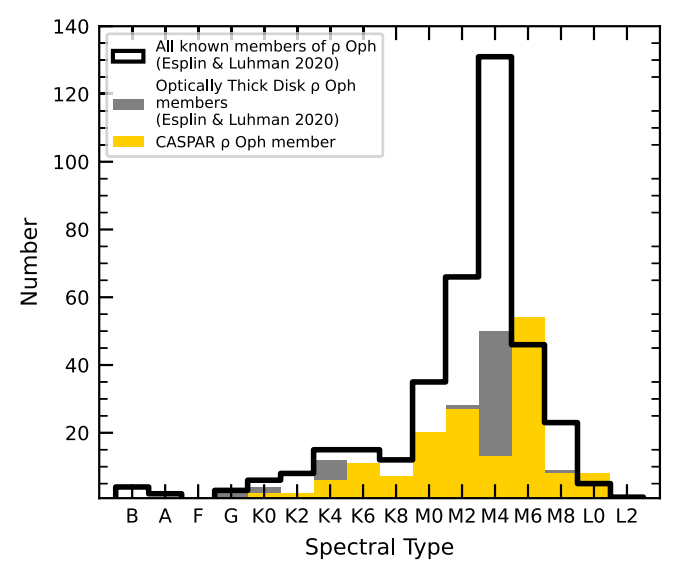


**Figure 3.** Distribution of spectral types in  $\rho$  Ophiuchus from the complete census survey (black) and systems with optically thick disks (gray) from Esplin & Luhman (2020; binned as in their Figure 22). Overlaid in yellow are the CASPAR  $\rho$  Ophiuchus objects.

Herczeg & Hillenbrand (2014) and Luhman et al. (2003), we find that they diverge by  $\sim 100-150$  K for M dwarfs, a change of  $\sim 0.06\,M_{\odot}$ , with the Herczeg & Hillenbrand (2014) temperatures found to be lower for the same spectral type. This results in the decrease in mass seen in CASPAR for these objects.

The objects are from 12 different SFRs and from 16 different original references, indicating no preferential biases in deriving masses. Under this uniform derivation, we find 658 stars, 130 BDs, and 10 PMCs (see Table 3).

The residuals between the CASPAR accretion rates and their literature-derived values are shown in Figure 6 for the full sample and each accretion diagnostic. Overall, we find that the  $1\sigma$  standard deviation in the residuals for all rederived accretion rates is 0.38 dex over the range of [-3.8, 1.15] dex (mean =-0.05 dex). We find that 909 (88%) of the accretion rates change by less than 0.5 dex, indicating the vast majority of the objects have not markedly changed from their literature value. We find that the most disparate changes in accretion-rate measurements are by  $H\alpha$  photometric luminosity and continuum excess, with CASPAR measurements larger than previously calculated. When we look at those accretion rates calculated from excess continuum, we find a median difference between the rederived and literature radius/mass ratio of

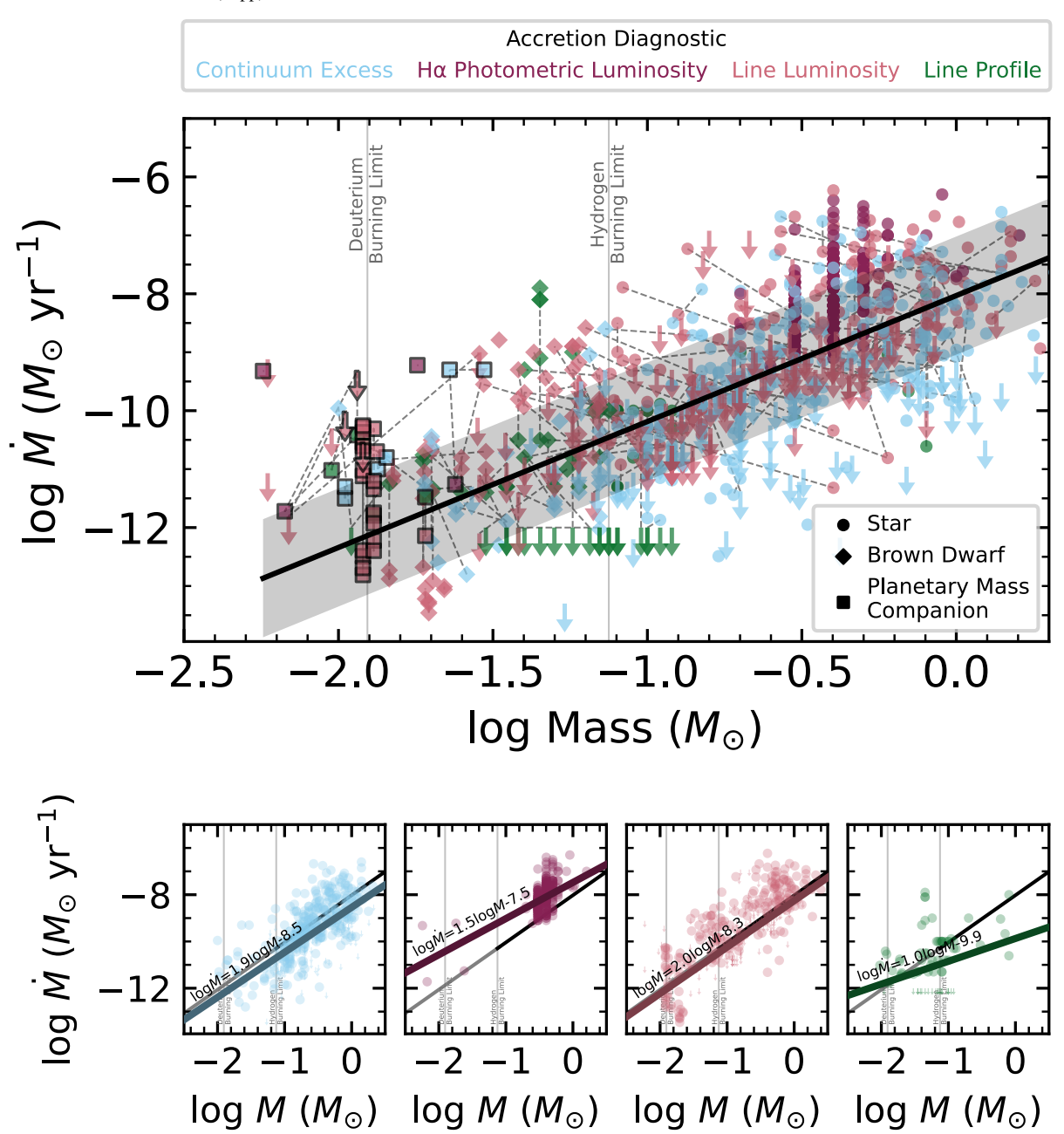


Figure 4. Literature Database of accreting objects. Top: accretion rate vs. mass colored by accretion diagnostic. The dashed gray lines indicate objects with multiple accretion-rate and mass estimates. The best-fit relation,  $\dot{M} \sim M^{2.16}$ , is shown with a black solid line, with the  $1\sigma$  upper limit in gray. Bound PMCs are indicated by thicker-edged squares, while stars are indicated by circles and BDs by diamonds. Upper limits are shown by downward arrows. Bottom: accretion rate vs. mass for separate accretion diagnostics—continuum excess (light blue), H $\alpha$  photometric luminosity (dark red), line luminosity (salmon), and line profile (green). The solid lines show the best fit for each diagnostic, with the black/gray line indicating the overall fit from the top panel. The vertical gray lines indicate the HBL and DBL. Overall, the literature database follows similar trends to previous surveys, while highlighting the strong scatter and variation in accretion rate and mass resulting from different methodologies.

0.3 dex. As these accretion-rate measurements are dependent on R/M ( $\dot{M} \propto R/M$ ), this in turn leads to a median difference between the rederived and literature  $\dot{M}$  of  $\sim$ 0.1 dex, indicating the majority of accretion rates derived from excess continuum are higher than originally estimated.

## 4. Linear Fitting Technique

With CASPAR, we can better investigate the causes of scatter in accretion rates. In the following sections, we discuss the relationship between the accretion rate and parameters such

as mass and age. Unless otherwise stated, these relationships are derived using the hierachical Bayesian linear regression routine linmix (Kelly 2007) in Python, <sup>16</sup> to determine the slope, intercept, and intrinsic scatter around relations of the form: y = mx + b. linmix allows for heteroscedastic and correlated measurement errors, and it takes upper limits into account. It assumes that x and y variables are drawn from a 2D Gaussian distribution, and the covariance matrix is composed of the uncertainties in x and y. Calculated regression

https://github.com/jmeyers314/linmix

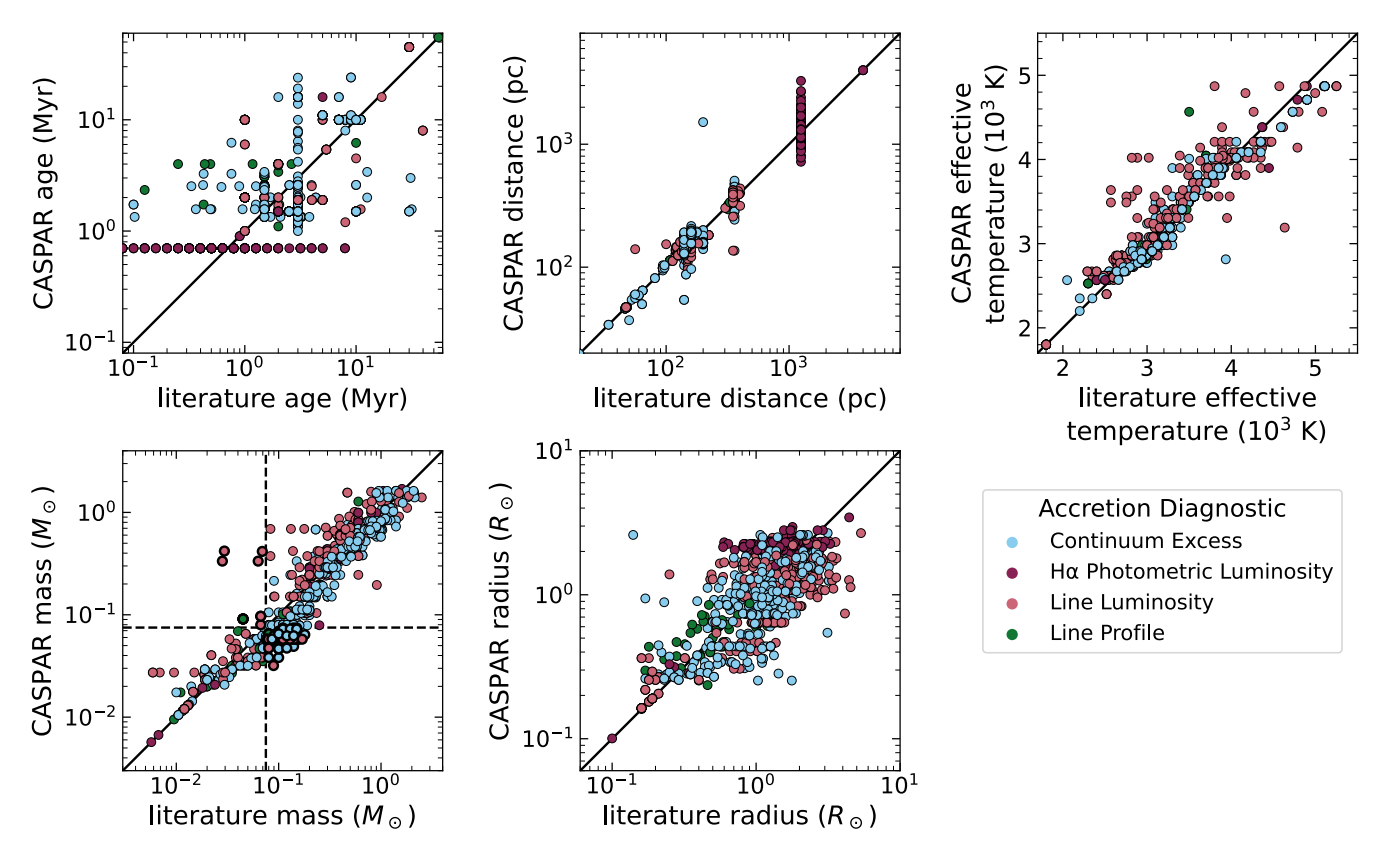


Figure 5. Comparison between the Literature Database physical parameters and those rederived in CASPAR colored by accretion diagnostic. The black line indicates 1–1. For masses, we show the HBL at  $M=0.075~M_{\odot}$  with the dashed black lines; under a uniform methodology, objects in the lower right quadrant decreased in mass from stellar to substellar, while in the upper left, the reverse occurred. We find 50%-89% of CASPAR parameters are within a factor of 2 of the literature value.

 Table 3

 Population Counts between Literature Database and CASPAR

Population	Literature Database	CASPAR
Star	712	658
BD	76	130
PMC	10	10

coefficients and uncertainties are derived from the posterior probability distributions of the model parameters computed using Markov Chain Monte Carlo.

Not every object in the Literature Database, and therefore CASPAR, has a reported  $\dot{M}$  uncertainty. For objects with no literature uncertainty, we assume the average  $\dot{M}$  uncertainty from all reported and rederived measurements in CASPAR ( $\sim$ 0.36 dex) in the fit.

For each fit performed, we recover the posterior distribution of the slopes and intercepts and calculate best-fit parameters from the median and  $1\sigma$  uncertainties. Additionally, we calculate the Pearson correlation coefficient, R, between the x and y parameters. Best-fit coefficients are recorded in Table 4.

In Appendix D, we discuss additional linear regression methods that were investigated, such as weighted least squares, ordinary least squares bisector, and orthogonal distance regression. We find that including upper limits in the fits does not significantly affect the best-fit coefficients. However, the inclusion of *x*-axis uncertainties can significantly affect the resulting best-fit coefficients.

For fits that do not follow y = mx + b (such as  $y = e^x$ ) and therefore cannot be fit with linmix, we utilize the orthogonal distance regression code scipy.odr, which allows for the fitting of nonlinear functional forms, while taking into account both x and y measurement uncertainties, but not upper limits (though this should not greatly affect the fit, as discussed above).

## 5. Effect of Methodology on Accretion-rate Scatter

CASPAR spans a wide range of masses from  $\sim 10~M_{\rm J}$  to  $\sim 2~M_{\odot}$  and compiles accretion rates calculated from four diagnostics. We first investigate (a) the extent to which a uniform derivation reduces the extensive scatter in  $\dot{M}$ , and (b) whether or not the accretion diagnostic influences this scatter.

## 5.1. Scatter in Accretion Rate after Rederivation

The relationship between the mass accretion rate and mass follows a power law of the form  $\dot{M} \propto M^{\alpha}$ , where previous measurements of  $\alpha$  range from 1.0 to 2.8 (e.g., Calvet et al. 2004; Natta et al. 2004; Mohanty et al. 2005; Muzerolle et al. 2005; Herczeg & Hillenbrand 2008; Zhou et al. 2014; Hartmann et al. 2016). Typical dispersions are 1–2 dex (Manara et al. 2023 and references therein). The top panel of Figure 4 shows the best fit to the Literature Database as  $\log \dot{M} = 2.16(\pm 0.08) \log M - 8.03(\pm 0.06)$ , with a  $1\sigma$  dispersion of 1.00 dex and correlation of 0.73. The wide range of previously measured stellar slopes is consistent with our

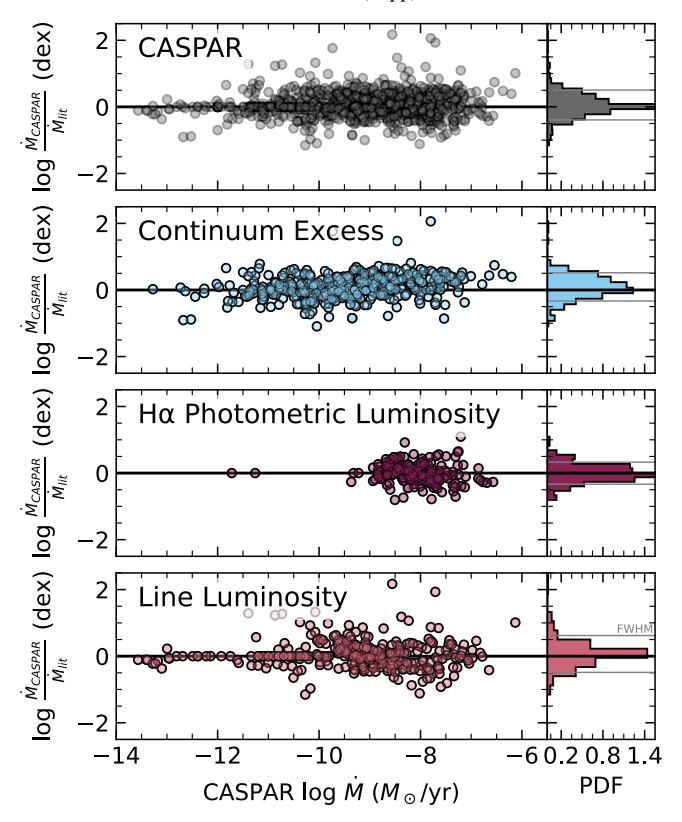


**Figure 6.** Residuals between reference and CASPAR accretion rates as a function of CASPAR accretion rate for different accretion diagnostics. 88% of all rederived values changed by less than 0.5 dex, with the line luminosity accretion diagnostic showing the most change in calculated accretion rate. Right: histograms of difference between literature and rederived accretion rates for each tracer. The thin gray lines indicate the FWHM. Colors as in Figure 5.

Literature Database fit and is likely driven by uncertainties in the masses and differences in sample ages and sizes (Hartmann et al. 2016).

Therefore, we first affirm that the rederived values in CASPAR are consistent with previous slope estimates and discuss how the scatter changes for a larger sample and under a uniform methodology. We show the best-fit model for CASPAR  $\dot{M}-M$  in Figure 7 and find a linear trend of

$$\log \dot{M} = 2.02(\pm 0.06)\log M - 8.02(\pm 0.05),\tag{2}$$

with a  $1\sigma$  dispersion of 0.85 dex and a strong correlation coefficient of 0.76.

CASPAR was based on previous studies; therefore, a consistent slope with literature estimates is unsurprising. A uniform derivation reduces the  $1\sigma$  dispersion by 0.15 dex, indicating that methodology accounts for only 17% of the original scatter. This implies that the remaining scatter is due to underlying physical mechanisms, rather than methodological systematics, and that methodology (e.g., object mass and radius estimation techniques, varied distance references, etc.), while accounting for some of the dispersion in the scatter, cannot explain all of it, especially as large scatter is seen in uniform SFR surveys (e.g., Manara et al. 2015; Alcalá et al. 2017).

In Figure 8, we also compare the best-fit  $\dot{M}$ –M relations from Zhou et al. (2014) and Hartmann et al. (2016) to CASPAR. Though we do not expect significant variation between our fit and previous estimates, the samples from Zhou et al. (2014) and Hartmann et al. (2016) were primarily

composed of stars between 0.1 and 1  $M_{\odot}$ , while our fit includes objects down to  $0.01 M_{\odot}$ . Therefore, we investigate whether the substellar population is different than previous stellar fits.

We compare the best-fit relation of (a) the CASPAR total sample and (b) the stellar sample to the fits of Hartmann et al. (2016) and Zhou et al. (2014). We find that the Zhou et al. (2014) and CASPAR star-only  $(0.075 < M/M_{\odot} < 1.7)$  fits show positively skewed residuals when extended into the BDs and PMC mass regimes, while the Hartmann et al. (2016) and CASPAR single-population fit show a positive skew only for PMCs (due to the stellar population dominating the fit). In the histograms of the residuals in Figure 8, we indicate the center of the distribution with a narrow gray line. We find that while the four fits overlap in the stellar regime, they deviate at substellar masses, with our fits accounting for most of the scatter, within fit uncertainties.

#### 5.2. Accretion Diagnostic Systematics

To assess the consistency among various observational methods, we assume that all methods should produce consistent  $\dot{M}$  values of estimating accretion rates. In Figure 9(a), we show CASPAR  $\dot{M}$ -M statistics separated by accretion diagnostic. We bin the accretion rates by mass to facilitate comparison. To do this, we assume every detection is a Gaussian probability density function (PDF) with a mean of the accretion rate and standard deviation of the uncertainty. For nondetections, we assume a half-normal distribution with the cutoff at the upperlimit value. We then run a Monte Carlo simulation drawing random values from the PDFs within each mass bin and take the median of the values. We find consistent median accretion rates for each mass bin across the four diagnostics, with the medians closely following the best-fit line found for continuum excess. Figure 9(b) shows the fit residuals. Though within uncertainties, H $\alpha$  photometric luminosities produce higher  $(\sim 1 \text{ dex}) \dot{M}$ s, while line profiles produce lower  $(\sim 1 \text{ dex})$  ones. However, the majority of the  $H\alpha$  photometric measurements are for objects with ages <1 Myr, biasing the results (see Section 6.1). Overall, line luminosity and continuum excess methods produce the smallest residuals in the stellar regime (residuals <0.4 dex) of the four diagnostics. As there are only 10 PMCs, in which the masses and accretion rates are not uniformly derived, we cannot conduct a similar analysis, though we show them in Figure 9.

We find line-profile-derived accretion rates lie consistently below the best-fit line for the substellar-mass objects, while continuum excess is consistent to within  $\sim$ 0.21 dex across all masses. For line luminosities, we find relatively small residuals (up to 0.8 dex) in the substellar regime. Though within uncertainties, line luminosity and line profile residuals trend upward from the stellar to substellar regime, while this is not seen for the accretion rates derived from the continuum excess tracers. The standard deviation of the residuals between the line luminosity and excess-continuum-derived rates increases from 0.1 dex at 0.5  $M_{\odot}$  to 0.65 dex at 0.03  $M_{\odot}$ .

As line luminosities are dependent on scaling relations (derived from excess continuum) to compute accretion rates, we expect similar trends among excess continuum and line-luminosity-derived  $\dot{M}$ s. While they are consistent within uncertainties, the average accretion rates do show differences at low masses, potentially a result of utilizing stellar scaling relations in the substellar regime. We discuss this hypothesis further in Section 7.

Table 4
Best-fit Parameters

		N <sup>a</sup>	$a~(\pm~{\rm err})$	b (± err)	$\sigma^{\dagger b}$	R
			$\dot{M} \sim M$ Fits	* (= 333)		
D 14	Total	1038	2.15 (0.08)	-8.03 (0.06)	1.01	0.73
By Mass	Star	837	2.69 (0.13)	-7.80 (0.07)	0.92	0.64
<b>5</b>	Continuum Excess	396	1.92(0.13)	-8.53(0.09)	0.87	0.66
By Accretion	$H\alpha$ Photometric Luminosity	223	1.54(0.19)	-7.47(0.08)	0.05	0.84
Diagnostic	Line Luminosity	346	1.99(0.11)	-8.24(0.12)	1.10	0.74
	Line Profile	73	0.96(0.46)	-9.87(0.60)	2.00	0.27
		CASPAR	$\dot{M} \sim M$ Fits			
	Total	1038	2.02 (0.06)	-8.02 (0.05)	0.85	0.76
	Star	764	2.17 (0.11)	-7.97(0.05)	0.74	0.63
	Star + BD	1000	2.12 (0.07)	-7.98(0.05)	0.85	0.76
By Mass	BD	236	3.19 (0.57)	-6.54 (0.80)	1.36	0.40
	BD + Planet	275	1.55 (0.37)	-8.75(0.55)	1.36	0.29
	Planet	38	0.25 (2.91)	-10.66 (5.64)	0.81	0.04
	Continuum Excess	396	1.87(0.11)	-8.31(0.09)	0.92	0.68
	$H\alpha$ Photometric Luminosity	223	1.25(0.18)	-7.69(0.06)	0.13	0.64
	Line Luminosity	346	1.76(0.10)	-8.34(0.11)	1.15	0.71
By Accretion	Line Profile	73	1.64(0.40)	-8.91(0.52)	1.56	0.46
Diagnostic	Balmer	1558	2.18 (0.04)	-7.81 (0.04)	0.51	0.85
	Pashen/Brackett/Pfund	644	1.40 (0.06)	-8.17(0.05)	0.37	0.77
	HeI	486	1.72 (0.07)	-8.09(0.07)	0.49	0.76
	CaII	412	1.74 (0.08)	-8.03(0.08)	0.41	0.80
	Total ≤1 Myr	231	2.13 (0.17)	-7.45(0.07)	0.13	0.85
	Total (1–3] Myr	578	1.78 (0.08)	-8.23(0.07)	0.91	0.69
	Total (3–8] Myr	59	1.51 (0.21)	-8.51(0.23)	0.78	0.73
	Total >8 Myr	169	1.64 (0.15)	-8.95(0.17)	1.20	0.67
By Age	Star ≤1 Myr	224	1.53 (0.40)	-7.61 (0.12)	0.14	0.45
and Mass	Star $(1-3]$ Myr	413	2.12 (0.14)	-8.11(0.18)	0.76	0.64
	Star (3–8] Myr	29	2.43 (0.66)	-8.21(0.32)	1.09	0.61
	Star >8 Myr	97	1.21 (0.31)	-9.12(0.21)	1.36	0.37
	BD ≤3 Myr	158	1.68 (0.79)	-8.41(1.10)	1.57	0.2
	BD (3-8] Myr	21	5.88 (4.64)	-3.06 (5.92)	0.77	0.46
	BD > 8 Myr	57	4.44 (0.76)	-5.20 (1.12)	0.64	0.68
		M	~ Age			
	Literature	1038	-0.84 (0.06)	-3.17 (0.38)	0.80	-0.46
	CASPAR	1038	-0.86(0.09)	-2.81(0.60)	0.77	-0.31

**Notes.** Linear fit in the form:  $\log \dot{M} = a \times X + b$ , where X is either  $\log M$   $(M_{\odot})$  or Age (Myr).

Accretion rates measured from line emission are known to have significant uncertainty, as scaling relations are empirically derived and many accretion-tracing lines can also be produced by other physical processes, such as winds and chromospheric activity (Jayawardhana et al. 2003; White & Basri 2003). Several criteria have been established to try to separate accretion and chromospheric activity using H $\alpha$  equivalent widths (<200 km s<sup>-1</sup>; Jayawardhana et al. 2003; White & Basri 2003) and the  $L_{\rm acc}/L$  ratio as a function of temperature (and spectral type) for emission lines (-3.19  $\pm$  0.15 for M6 dwarfs; Manara et al. 2017b).

In Figure 10, we group line fluxes by wavelength—namely: (a) Balmer series; (b) IR hydrogen series (Paschen, Brackett and Pfund); (c) Helium I emission lines (He I  $\lambda$  4026, He I  $\lambda$  4471, He I  $\lambda$  4713, He I  $\lambda$  5016, He I  $\lambda$  5876, He I  $\lambda$  6678, and He I  $\lambda$  7065); and (d) Calcium II emission lines (Ca II K, Ca II H, Ca II  $\lambda$  8498, Ca II  $\lambda$  8542, and Ca II  $\lambda$  8662)—in order to analyze trends among

them. We first find best-fit  $\dot{M}$ –M relations for each line flux group (given in Table 4) and compare these fits to the CASPAR best-fit relation. We use the Akaike information criterion (AIC) to access the performance of the linear fits in explaining the variation in the data.<sup>17</sup> Since our two fits are independent (i.e., non-nested) with the same number of parameters, this criterion estimates how well the model reproduces the data from the maximum likelihood.

If the AIC values for two fits are within 10%, we consider the fits to be comparable. If the fit to a line flux group is not significantly more descriptive of the variance than the overall best-fit relation, we conclude that offsets by method do not

<sup>&</sup>lt;sup>a</sup> N refers to the number of  $\dot{M}$  measurements.

<sup>&</sup>lt;sup>b</sup> Standard deviation of the linear fit.

 $<sup>\</sup>overline{}^{17}$  The AIC, defined as AIC =2 $k-2\ln(L)$ , informs the relative quality of different models against a given set of data, where k is the number of estimated model parameters and L is the likelihood function of the model.

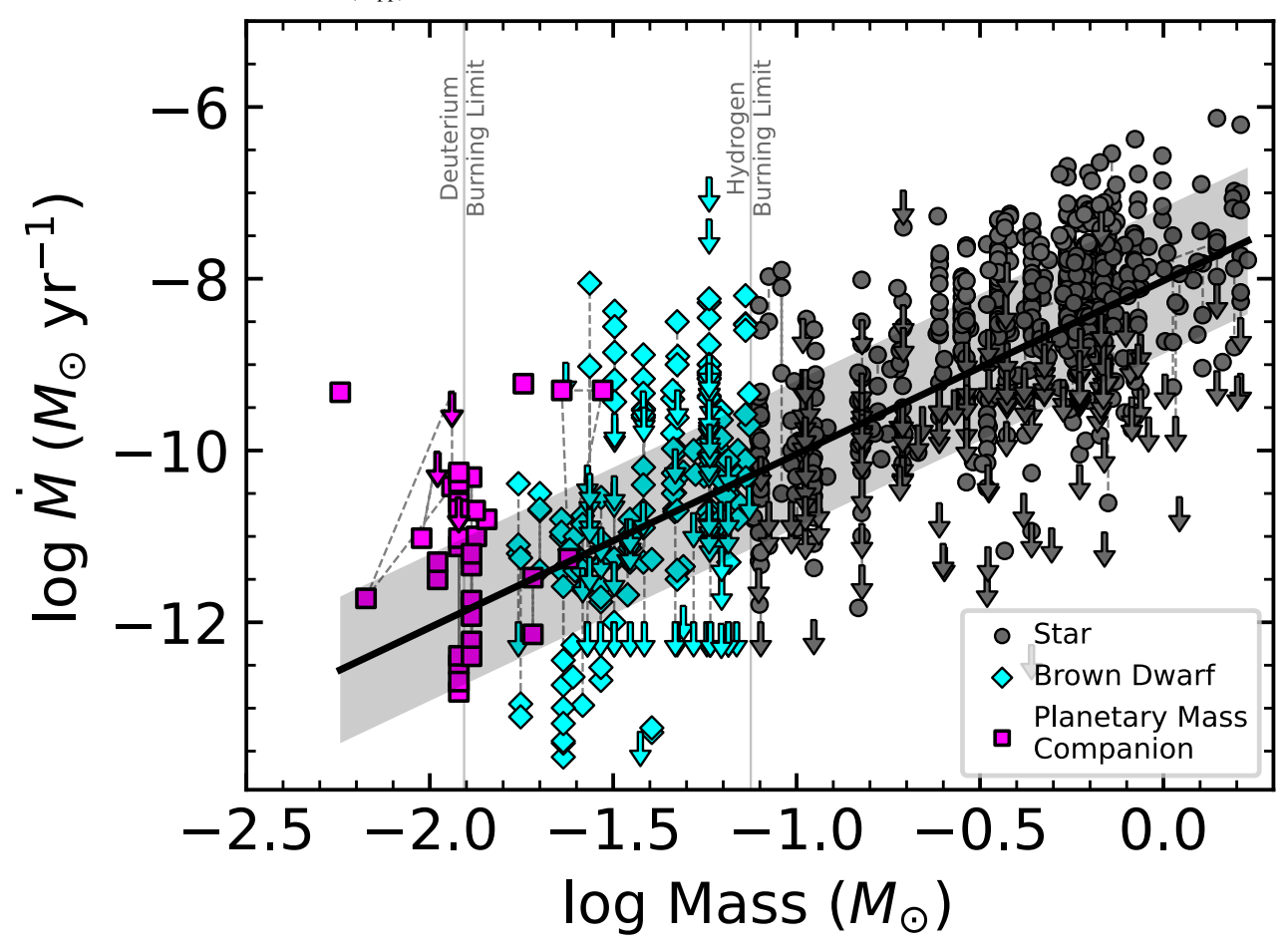


Figure 7. The CASPAR  $\dot{M}-\dot{M}$  relation for stars (black circles), BDs (cyan diamonds), and PMCs (magenta squares). The gray dashed lines show accretion rates derived for the same object, and the downward arrows show accretion-rate upper limits. The black line and shaded region shows our best linear fit,  $\log \dot{M} = 2.02 \log M - 8.02$ , and  $1\sigma$  dispersion,  $\sigma = 0.85$  dex ( $\dot{M}$  in  $M_{\odot}$  yr<sup>-1</sup> and M in  $M_{\odot}$ ), to all accretion rates in CASPAR.

contribute to the scatter. In the stellar regime, we find the AICs for each line flux group are all within 10%.

In the substellar regime, the best-fit line to the IR hydrogen and He I line measurements is offset from the overall best fit with a percent difference between AIC  $\sim\!\!180\%$ . Additionally, at the deuterium-burning limit (DBL), the near-IR (NIR) best-fit line is offset from the CASPAR best fit by 0.9 dex (compared to  $<\!0.4$  dex for the other lines). This could indicate that the NIR line flux scaling relations overestimate accretion rates in the substellar regime (i.e., their scaling relations are different) or this may result from small number statistics.

Finally, we estimate the extent to which accretion rates derived from  ${\rm H}\alpha$  10% widths,  ${\rm H}\alpha$  line profiles, and UV excess differ in order to probe their effect on scatter. When accretion rates are derived from different emission lines or continuum at the same epoch, they should not be subject to intrinsic accretion variability. This makes contemporaneous measurements an excellent probe of systematics. While  $\dot{M}s$  from  ${\rm H}\alpha$  luminosity rely on  $L_{\rm line}-L_{\rm acc}$  scaling relations, the  $\dot{M}-{\rm H}\alpha$  10% width scaling relation of Natta et al. (2004) relates the 10% width directly to the accretion rate. However, Alcalá et al. (2014) found that it can underestimate accretion rates by almost 0.6 dex for widths <400 km s<sup>-1</sup> in Lupus (corresponding to  $M<0.3~M_{\odot}$ ) compared to excess continuum. We find a similar

result when we compare the CASPAR  $H\alpha$  10% widths to accretion rates derived from excess continuum.

In Figure 11, we show the residuals in CASPAR accretion rates derived from excess continuum (top) and  $H\alpha$  10% width (bottom) compared to simultaneous measurements from  $H\alpha$  luminosity as a function of mass. In the stellar regime, accretion rates derived from these three quantities do not significantly differ within 1 dex. In the substellar regime, accretion rates derived from  $H\alpha$  luminosity are systematically high when compared to excess continuum, which could be indicative of an overestimation of accretion luminosity for the lowest-mass BDs and PMCs.

We find a large offset in accretion rates derived from  $H\alpha$  10% width compared to  $H\alpha$  luminosity. Several other processes, including chromospheric activity, outflows, and hotspots, contribute to  $H\alpha$  emission, potentially inflating its width and therefore increasing its inferred accretion rate. Low-mass substellar accreting objects can have line widths below the traditional 200 km s<sup>-1</sup> threshold for accretion. Such observations have led previous work (e.g., Alcalá et al. 2014, 2017) to discourage the use of  $H\alpha$  10% width as an accretion tracer. We confirm this offset between  $H\alpha$  10% width and  $H\alpha$  luminosity within the substellar regime and find it can lead to a difference of almost 2 dex in calculated accretion rate near the DBL, producing vastly overestimated accretion rates.

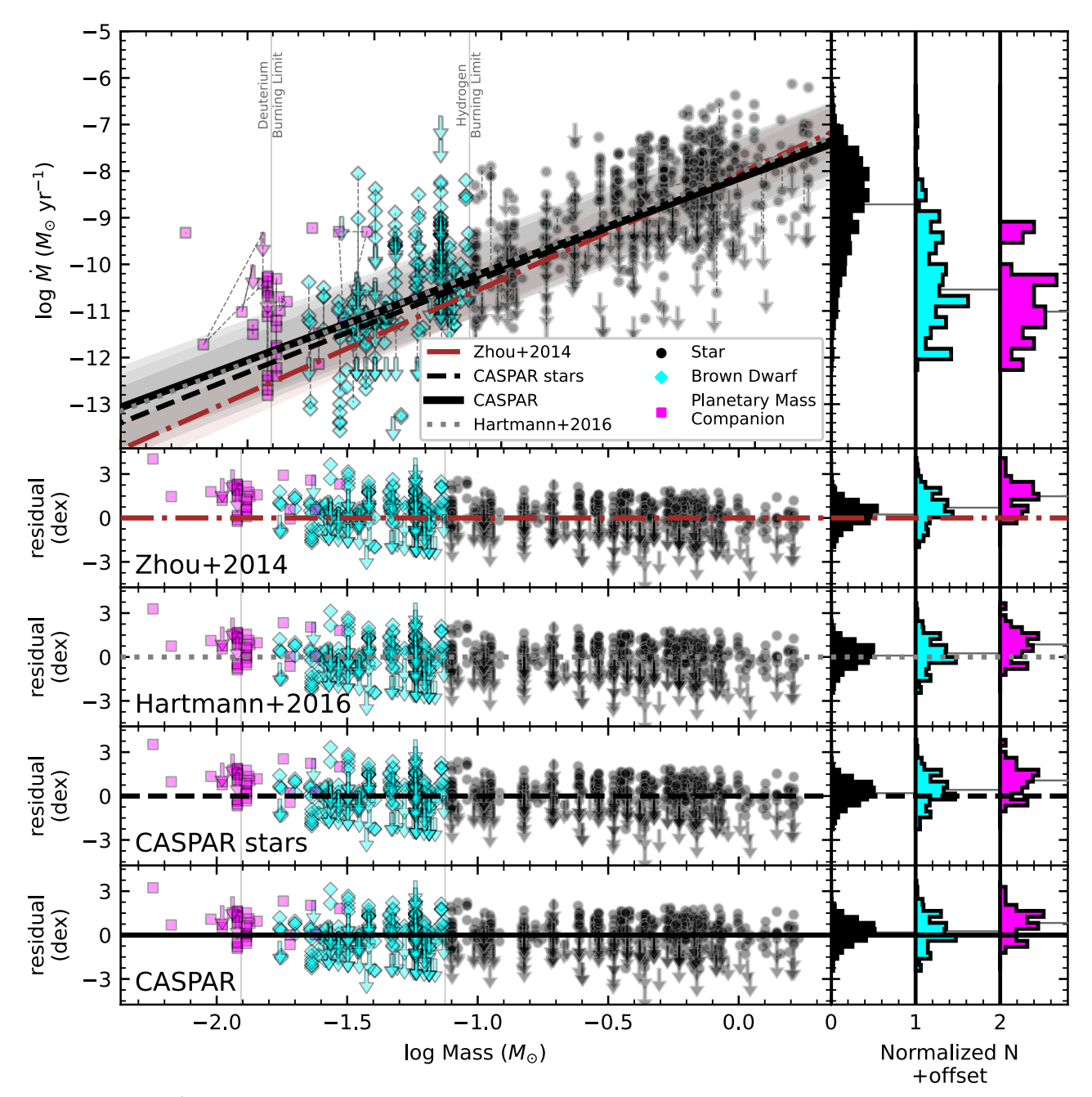


Figure 8. Left: the CASPAR  $\dot{M}$ –M best-fit relation for overall CASPAR (black solid line), CASPAR stars only (black dashed dot line), Zhou et al. (2014; gray dotted line), and Hartmann et al. (2016; brown solid line). The  $1\sigma$  scatter is shown by the shaded regions for each fit. The residuals between each linear fit and CASPAR are shown below. Right: histogram of residuals for each population. The thin gray lines show the mean of each distribution. Markers and colors are as in Figure 7.

## 5.3. Summary

We find that methodological differences in estimates of mass accretion rates, such as differences in evolutionary models and estimated distances (used to scale accretion luminosities), account for only  $\sim 17\%$  of the scatter in the  $\dot{M}-M$  relation, indicating that the remaining scatter is from either observed accretion diagnostic systematics or physical differences (e.g., variability, disk mass, stellar mass, and system age).

When we separate accretion-rate estimates by accretion diagnostic, we find that accretion rates do not vary significantly (<1 dex) in the stellar or substellar regimes. However, we do find systematically higher accretion rates for  $\dot{M}$ s derived from NIR line luminosities (a 0.9 dex offset in the best-fit line at the

DBL; Figure 10(b)) and  $H\alpha$  luminosity relative to continuum estimates (top panel of Figure 11). We will discuss the physical and diagnostic drivers of this scatter in the following sections.

## 6. Drivers of Physical Scatter in Mass Accretion

As shown in the previous section, methodological systematics cannot fully explain the scatter in the  $\dot{M}-M$  relation for either stellar or substellar objects. Recent work has suggested that multiplicity may affect accretion rates, with binaries accreting at a higher rate than isolated objects (Gangi et al. 2022; Zagaria et al. 2022). While CASPAR currently does not contain many objects in multiple systems (46/798), they appear consistent with isolated object accretion rates and do not

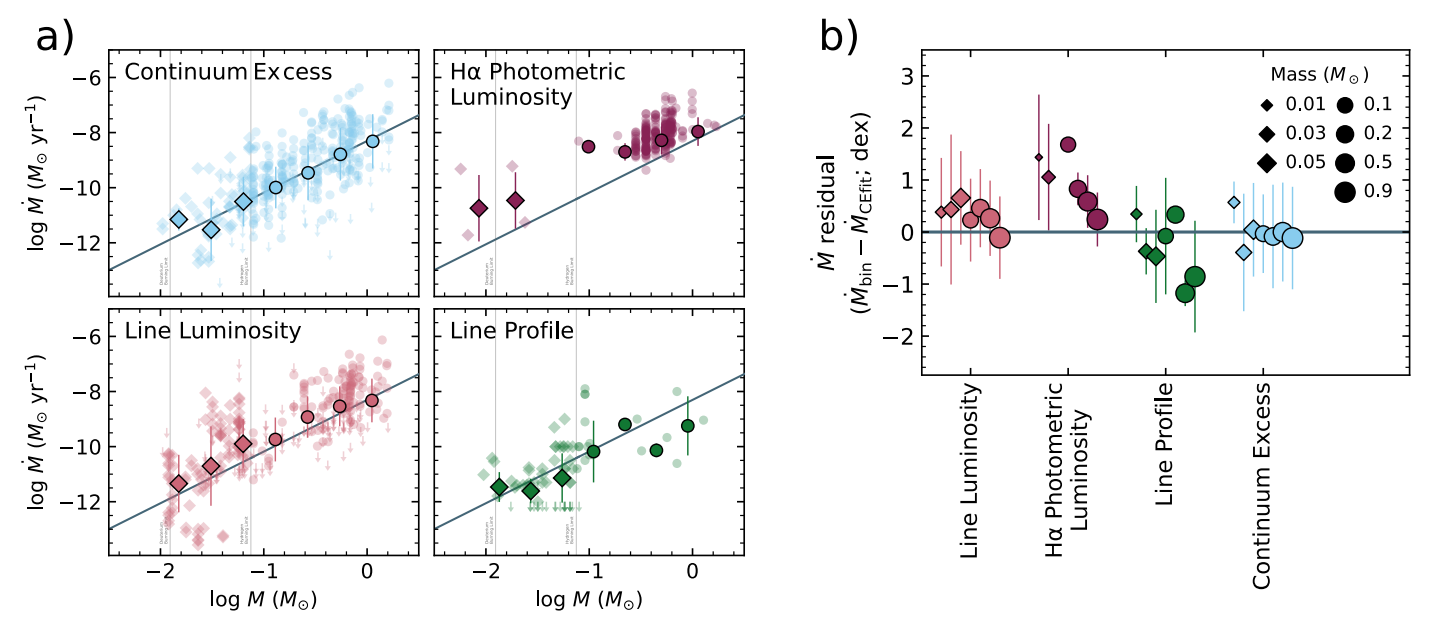


Figure 9. (a) Accretion rate vs. mass for individual accretion diagnostics, colored as in Figure 4. The large markers indicate the binned accretion rates by mass. (b) Residuals between binned accretion rates and CASPAR continuum excess fit. The line luminosities (including  $H\alpha$  photometric) show (significant) deviation from the continuum excess with decreasing mass. The  $H\alpha$  photometric luminosities appear significantly offset from the CASPAR continuum excess best fit; however, the majority of the stellar accretion rates are from objects with ages <1 Myr, which biases the high-mass results (see Section 6.1).

have a significant effect on the  $\dot{M}-M$  scatter. Below, we focus on the relationship between age and intrinsic variability in the observed  $\dot{M}-M$  scatter<sup>18</sup> and what this may tell us about the evolution of accretion activity.

## 6.1. Variation in Accretion with Age

Circumstellar disk fraction in young SFRs has been found to decrease exponentially with age until  $\sim 10-15$  Myr (Mamajek 2009; Luhman 2022), with the majority of disks dissipating after  $\sim 2.5$  Myr. The rate of decay is mass-dependent, as Luhman (2022) found an increase in disk fraction with decreasing mass in the 15–21 Myr Lower Centaurus Crux and Upper Centaurus Lupus associations. They found that the lower-mass objects retained their disks longer than the previously presumed disk dispersal timescales of 10-15 Myr.

Correlations among accretion rates, disk gas masses, and accretion timescales (Hartmann 1998; Manara et al. 2016b; Mulders et al. 2017) are generally explained through a combination of viscous evolution (Lodato et al. 2017; Mulders et al. 2017; Rosotti et al. 2017), disk photoevaporation (Sellek et al. 2020), and stellar multiplicity (Zagaria et al. 2022). Accretion rates decrease with time as  $t^{\alpha}$ , where  $\alpha = -1.6$  to -1.2 (Hartmann et al. 2016 and references therein). This decrease has been attributed to viscous evolution, though observations of the POISSON sample found higher  $\dot{M}$  than expected from pure viscous models (Antoniucci et al. 2014).

By establishing a "uniform" estimate of ages, we can study the correlation of  $\dot{M}$  with age and its impact on  $\dot{M}$ -M scatter. We exclude PMCs in this analysis, as (a) they have not been uniformly rederived, and (b) theoretically modeled accretion (Aoyama et al. 2018; Thanathibodee et al. 2019; Aoyama et al. 2020) and formation (Stamatellos & Herczeg 2015) mechanisms posit that stellar age trends could not hold for PMCs. We divide CASPAR into the following four age bins for this analysis:

- 1. ≤1 Myr: includes the Lagoon Nebula;
- 2.  $1 < t/Myr \le 3$ : includes Chamaeleon I, Taurus, and Lupus;
- 3.  $3 < t/Myr \le 8$ : includes IC 348 and Perseus; and
- 4. >8 Myr: includes Upper Centaurus Lupus and  $\eta$  Chamaeleontis.

See Table 7 for the full list of ages for each cluster and association within these broad groups.

In Figure 12, we show accretion rate as a function of age, colored by stellar mass. Following Hartmann et al. (2016), we scale the accretion rate to  $M_* = 0.7\,M_\odot$  in order to remove the dependence on mass. The best fit to these data using linmix is

$$\log \frac{\dot{M}}{M_{\odot}/\text{yr}} = -0.85(\pm 0.09) - 2.80(\pm 0.60) \times \log \frac{t}{\text{yr}}, \quad (3)$$

with a scatter of 0.77 dex and Pearson correlation coefficient of -0.31. The slope found by Hartmann et al. (2016; slope =-1.07) shows a faster decline in accretion rate with age compared to the CASPAR slope. The sample of Hartmann et al. (2016) consisted of 148 objects whose accretion rates were computed from continuum excess and line emission with ages of  $5 < \log t/\text{year} < 6$ . This smaller sample size and age range could account for the difference in fit.

As a simple test of the effect of age, we begin by assuming that objects, no matter their age, share the same  $\dot{M} \sim M^{2.02}$  slope. For older objects, the accretion rates should be lower, resulting from a decrease in available disk material. We can model this simplified assumption as a decrease in the intercept

Though disk mass has a known correlation with accretion rate (Manara et al. 2023 and references therein), and modeling work has suggested that variations in accretion rates are due to differences in disk mass (Vorobyov & Basu 2009), disk masses are not currently collected in CASPAR. We crossmatch CASPAR with the sample from Manara et al. (2023) and reproduce the Manara et al. (2023) results comparing their disk masses with CASPAR stellar masses, ages, and accretion rates. Therefore, we focus here on quantifying age and multiepoch variability.

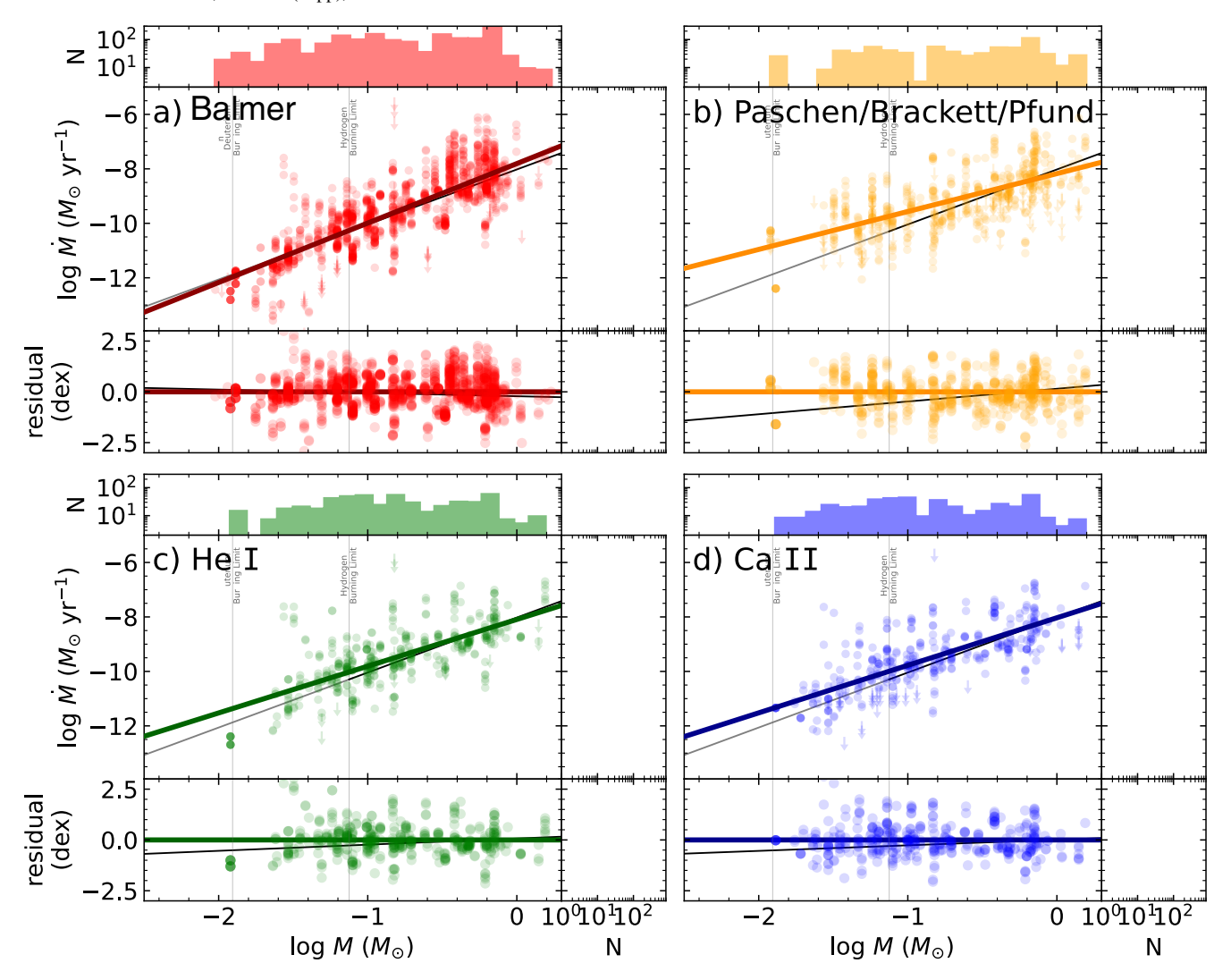


Figure 10. Accretion rate vs. mass for a range of accretion-tracing lines, namely: (a) optical Hydrogen Balmer series lines; (b) NIR Hydrogen Paschen, Brackett, and Pfund series lines; (c) Helium I emission lines; and (d) Calcium II emission lines. The gray line shows the best linear  $\dot{M}-M$  fit to the overall CASPAR database, while the colored lines show the best linear fit for each emission line. The histograms show the posterior distributions for the masses (top), accretion rates (top right), and accretion-rate residuals (bottom right) for each panel. We find that the NIR line flux fit shows the most deviation in best fit; it is offset by 0.9 dex compared to the best linear fit at the DBL (compared to <0.4 in the other lines).

of the  $\log \dot{M} - \log M$  relation with increasing age. This allows us to quantify the extent to which age affects the dispersion in the  $\dot{M}-M$  relation.

As shown in Figure 13, we find that the intercept decreases by 1 dex from <1 Myr to >8 Myr. Subtracting age best fits from each age population and overplotting the residuals gives an indication of the effect of age on overall scatter. If the scatter in  $\dot{M}$  for objects of the same mass is a result of age, then we expect the overall dispersion to decrease when age is accounted for in this way. However, we find from these residuals that the  $1\sigma$  scatter only decreases by 0.06 dex (bottom panel of Figure 13). While there is almost a 1 dex decrease in best-fit intercepts by age bin, the median scatter remains high. Therefore, as the dispersion within each age bin is roughly the same as the overall scatter, this normalization by age has an insignificant effect.

In the substellar regime, age has even less an effect on the overall scatter; we find the standard deviation of the residuals decreases by 7%. From Figure 8, the residuals in the substellar regime are positively skewed, exacerbating this effect in the age  $\dot{M}$ –M residuals, especially for the <1 and (3–8] Myr

regimes. This could indicate that substellar objects are following a different trend with mass or age. We investigate this hypothesis in Section 7.

## 6.2. Multiepoch Variability

Previous surveys (Biazzo et al. 2014; Costigan et al. 2014; Venuti et al. 2014) have primarily focused on day-to-day intrinsic accretion variability utilizing one accretion diagnostic. This variability produces a  $\sim$ 0.4 dex dispersion, smaller than the 1–2 dex observed in the  $\dot{M}$ –M relation. The variability is therefore not the dominant source of scatter in the  $\dot{M}$ –M relation for a given mass. However, CASPAR contains objects that have been observed from many different tracers across months and years. In this section, we quantify how this longer-timescale and methodological accretion variability affects the dispersion we see in the CASPAR  $\dot{M}$ –M relation.

We first look at all sources of variability, including the variation in accretion rates from different lines in the same epoch and the variation in accretion rate from the same line over multiple epochs. The median separation in measurements

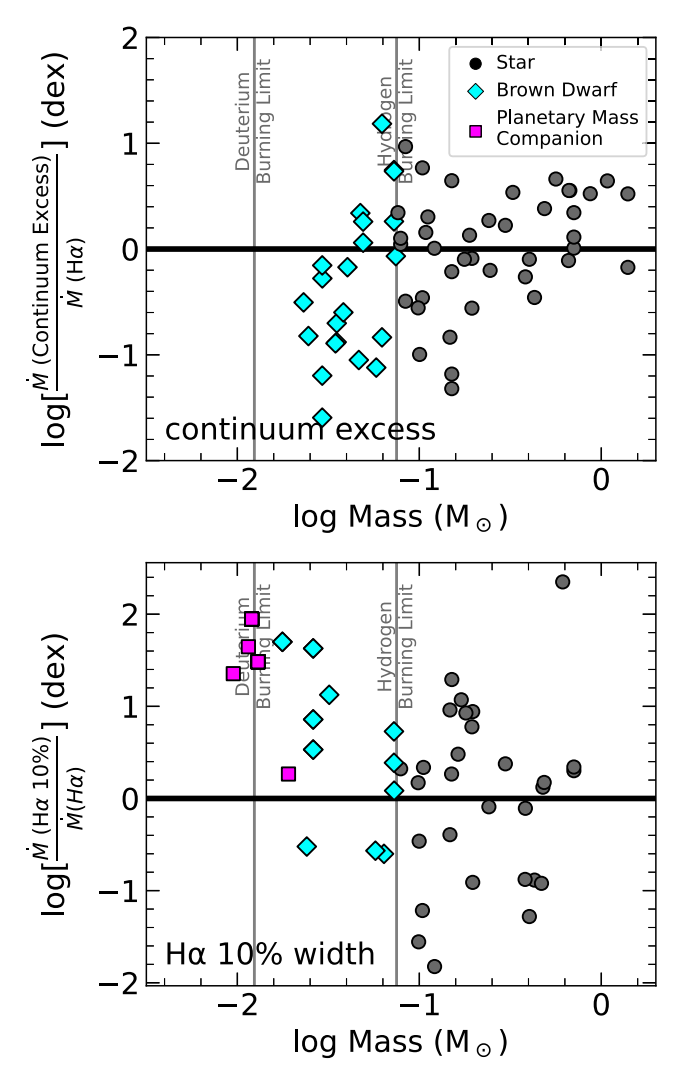
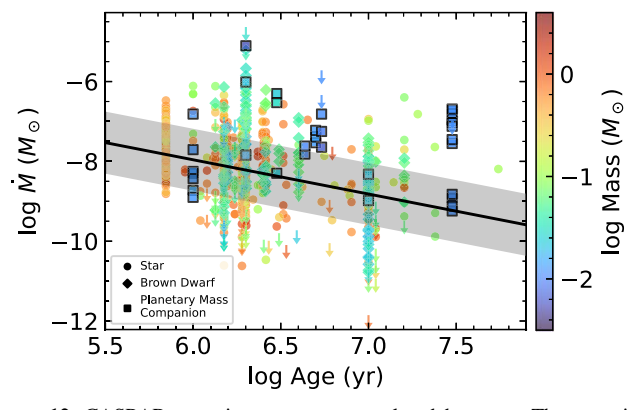


Figure 11. Difference in accretion rates derived from excess continuum (top) and H $\alpha$  10% width (bottom) compared to H $\alpha$  luminosity as a function of mass for objects with simultaneous H $\alpha$  luminosity and either excess continuum or H $\alpha$  10% width. As mass decreases, we find an offset in accretion rate between these quantities. Accretion rates derived from these simultaneous observations should not physically vary, thereby underscoring systematic methodological differences in calculating accretion rates.



**Figure 12.** CASPAR accretion rate vs. age colored by mass. The accretion rates have been scaled by the  $\dot{M}-M$  relation to  $M\sim0.7\,M_{\odot}$ , following Hartmann et al. (2016). The black line and shaded region show the best linear fit and  $1\sigma$  scatter.

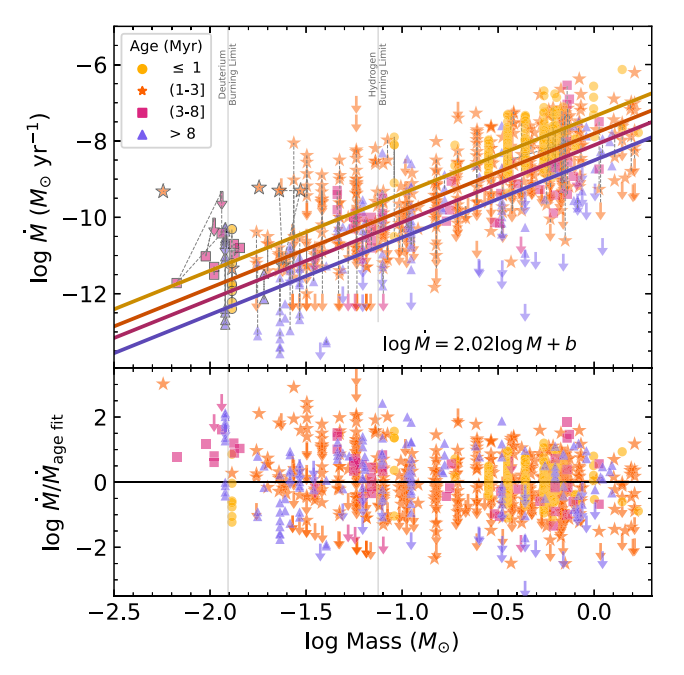
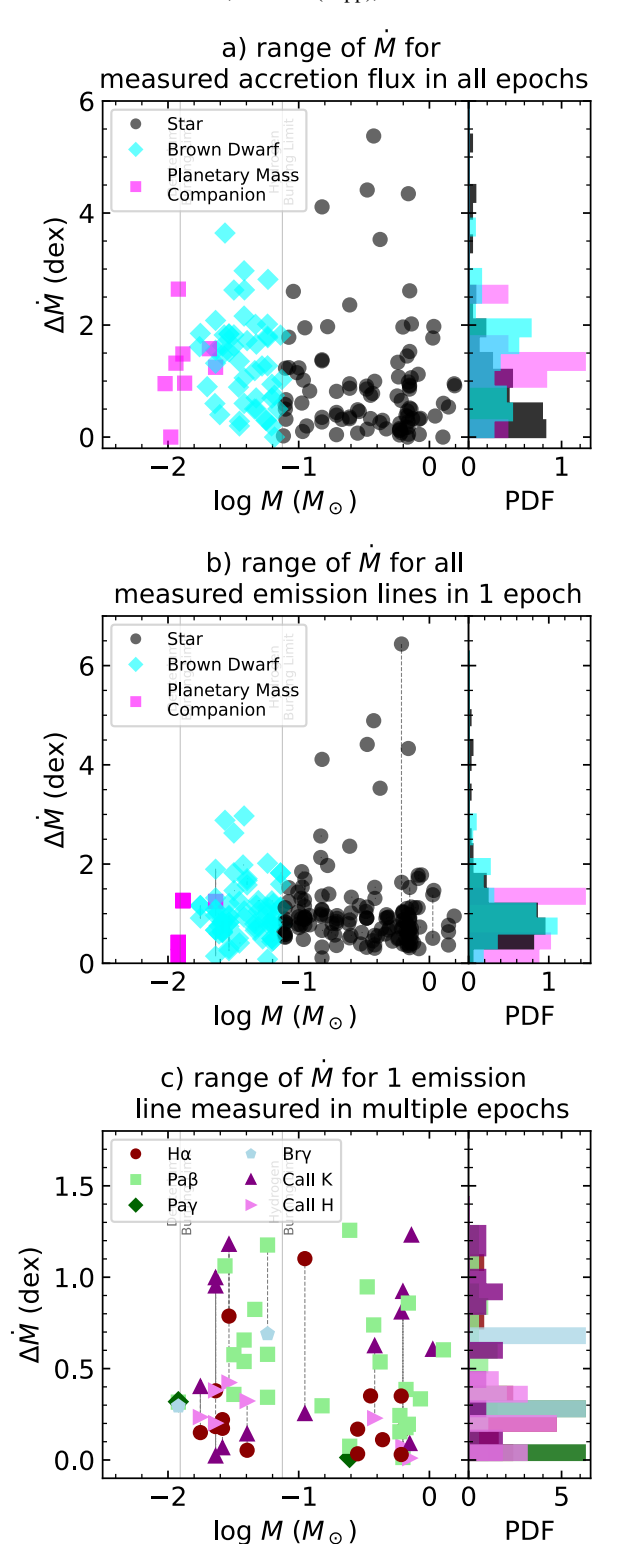


Figure 13. Top: CASPAR accretion rate vs. mass, colored by age:  $\leq 1$  Myr (gold circles), (1–3] Myr (orange stars), (3–8] Myr (magenta squares), and >8 Myr (purple triangles). The solid lines are the best linear fits to each age population with a fixed constant slope of 2.02. We find a 1 dex decrease in the best-fit intercept with increasing age. Bottom: residuals for the best linear fit for each age population.

is 3 yr, with a maximum separation of 21 yr, from Gullbring et al. (1998) to Alcalá et al. (2021). Overall, we find a spread of 0.63 dex in the stellar regime, which includes several high-variability outliers from multiline measurements from a single epoch (see Figure 14(a)) and which increases in the substellar regime to a median of 1.33 dex. We compute an independent two-sample student's t-test and find a significant (t (134) = 2.08, p = 0.03) difference in variability between the stellar (mean =1.00 dex,  $\sigma$  = 1.21 dex) and substellar (mean = 1.35 dex,  $\sigma$  = 0.78 dex) populations. This increase in variability could be indicative of either intrinsic variation resulting from the rotation of sunspots or accretion flows in the line of sight or from differences in diagnostics.

We also analyze two main sources of observed variation separately, namely: (a) variation among accretion rates measured from multiple lines at one observational epoch ("methodological"; 241 objects, Figure 14(b)); and (b) variation among accretion rates for one line observed at multiple epochs ("intrinsic"; 67 objects, Figure 14(c)). See Table 5 for the full breakdown of objects. We find that both the median methodological and intrinsic variation in accretion rate is on average 0.86 dex, double the amount of variability found in previous surveys. The methodological variability in  $\dot{M}$ determination is relatively consistent with mass, but we do note some strongly variable outliers. We find these objects show small (<1.5–2 dex) variability over multidecade time spans using a single accretion tracer, but have large (>3 dex) variation between accretion rates measured for different lines, with the largest outliers found in the Ophiuchus SFR (3.5-5.5 dex). The object with the most extreme multiline variability is DO Tau, which has a relatively stable accretion rate of  $10^{-8}\,M_\odot\,{\rm yr}^{-1}$ . However, Alcalá et al. (2021) found an H $\alpha$  line flux of  $1.92(\pm0.07)~{\rm e}{-17}~{\rm erg~s}^{-1}~{\rm cm}^{-2}$ , corresponding to an



**Figure 14.** Range of measured accretion rates for objects in CASPAR with (a) multiepoch/multiaccretion tracer measurements, (b) all accretion rates measured for all emission lines in one epoch, and (c) all accretion rates in all epochs for individual emission lines. In panels (a) and (b), the ranges are colored by stellar/substellar populations. In panel (c), the ranges are colored by the individual line tracers. The right panels shows the PDFs for each population. Overall, we find increased variability in the substellar regime (1.33 dex), but consistent 0.8 dex variability with population for emission lines and epochs.

**Table 5**Multiepoch Line Variability

Line	Number of Objects	Number of Multiepoch Observations	$\Delta \dot{M}$
$\overline{H\alpha}$	374	16	1.10
$Pa\beta$	207	25	1.26
$Pa\gamma$	141	2	0.32
$Br\gamma$	99	2	0.69
Ca II K	151	14	1.23
Ca II H	103	8	0.42

accretion rate of  $6.45 \times 10^{-15} M_{\odot} \text{ yr}^{-1}$  in CASPAR, a >7 dex difference in  $\dot{M}$ .

For intrinsic variation, we find  $Pa\beta$  and Ca II K produce the highest amounts of variability (1.26 dex and 1.23 dex, respectively), though small sample sizes affect the measured ranges of variability. For  $Pa\beta$ , we find the median variability increases from the stellar (0.33 dex) to substellar (0.57 dex) regimes, though this difference is not statistically significant ( $t=-1.42,\ p=0.16$ ), and as shown by Claes et al. (2022), measurements found from line luminosity can underestimate the variability for CTTSs.

Though no significant mass trends were seen for either methodological or intrinsic variation considered separately, when all sources of variation are considered together, we find a significant increase in the variability of  $\dot{M}$  in the substellar regime. As we show in Figures 9(b) and 10, while excess continuum accretion measures remain relatively constant with mass, accretion rates derived from line fluxes, particularly Pa $\beta$ , appear to deviate more from the  $\dot{M}$ -M relation as mass decreases.

For objects derived from both excess continuum and line flux, there could be as much as a 0.9 dex difference with  $\dot{M}$  estimates. This may point to physical differences in accretion processes in the substellar population (e.g., more luminosity in certain emission lines compared to the expectation from stars) that are not accounted for in current  $L_{\rm line} \sim L_{\rm acc}$  scaling relations. This could have a large impact on our interpretation of ongoing accretion and variability in the lowest-mass objects (S. K. Betti et al. 2023, in preparation).

#### 7. Role of Accretion on Substellar Formation

In Sections 5.2 and 6.1, we find offsets and skewed residuals in the  $\dot{M}-M$  relation for the substellar regime according to age, line tracers, as well as from the overall best linear fit, which might point to underlying differences in the  $\dot{M}-M$  relations needed to describe the stellar and substellar populations. Therefore, we explore whether the accretion rates of BDs are statistically distinct from stars and whether this can be connected to their accretion or formation mechanisms. If BDs are accreting differently, this could appear as differences in their calculated accretion rates.

When we fit each population (stars, BDs, and PMCs; hereafter, mass populations) separately, we find three distinct relationships, shown in Figure 15 and described by the following best-fit relations (hereafter, three population fits). For the stellar population, we find

$$\log \dot{M} = 2.18(\pm 0.11)\log M - 7.97(\pm 0.05),\tag{4}$$

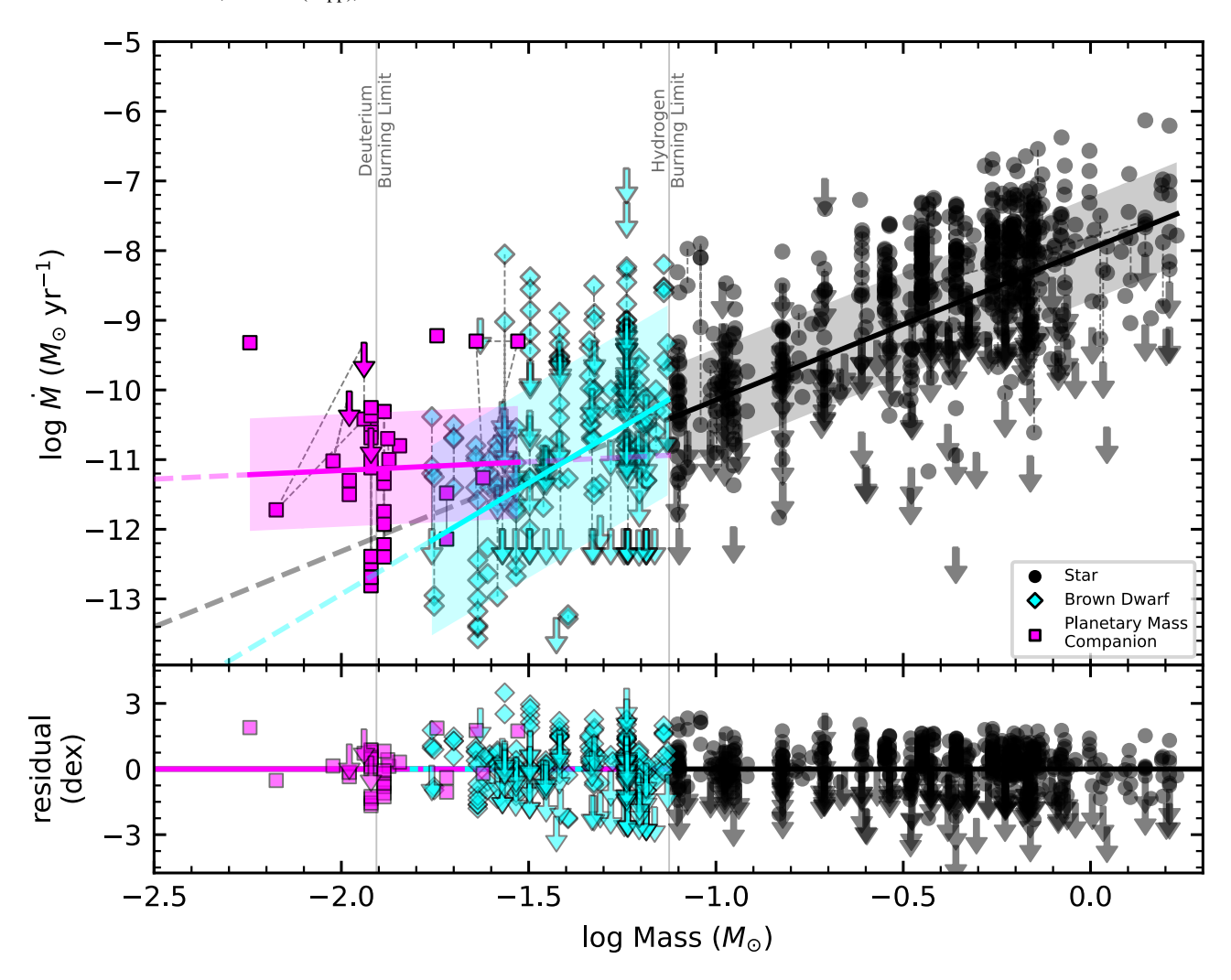


**Figure 15.** CASPAR  $\dot{M}-M$  best-fit relations for stars (black circles), BDs (cyan diamonds), and PMCs (magenta squares). The solid lines and bands show the best linear fit and  $1\sigma$  standard deviation of the fit for each mass population, while the dashed lines show extrapolations beyond the bounds of the fit regions. The bottom panel shows the residuals for each best fit. Downward arrows indicate accretion-rate upper limits.

with a residual standard deviation of 0.74 dex. The accretion rate,  $\dot{M}$ , is in  $M_{\odot}$  yr<sup>-1</sup> and M in  $M_{\odot}$ . For the BDs, we find

$$\log \dot{M} = 3.19(\pm 0.57)\log M - 6.54(\pm 0.80),\tag{5}$$

with a residual standard deviation of 1.36 dex. Finally, for the PMCs, we find

$$\log \dot{M} = 0.25(\pm 2.91)\log M - 10.66(\pm 5.64),\tag{6}$$

with a residual standard deviation of 0.81 dex. The stellar fit (slope = 2.18) is similar to those found by other authors (e.g., Calvet et al. 2004; Natta et al. 2004; Mohanty et al. 2005; Muzerolle et al. 2005; Herczeg & Hillenbrand 2008; Zhou et al. 2014; Hartmann et al. 2016), as discussed in Section 5.1.

For BDs, the slope of the relation steepens to 3.19 in the substellar regime, while the PMCs are best modeled by a flat dependence with mass. In Appendix E, we compare the three population fits to the single-population best fit described in Section 5.1, and find that separate fits are statistically favored over the single-population fit with lower AIC statistics.

This steeper slope ("knee") in the substellar/low-mass star regime has only been seen observationally in older individual star-forming systems (Alcalá et al. 2017; Manara et al. 2017a).

As CASPAR includes multiple SFRs at different ages, this steeper BD slope could be a result of these older ages having a stronger effect on the best-fit  $\dot{M}$ –M relation for this mass regime. Therefore, in the following sections, we explore the effects of mass with age and mass population in explaining both the scatter and evolution of BD accretion.

## 7.1. Effect of Age on BD Properties

Following the process outlined in Section 6.1, we explore the effect of age in explaining the  $\dot{M}$ -M relation for substellar objects. We combine the original <1 Myr and (1-3] Myr populations due to small numbers within the <1 Myr bin. As shown in Figure 16, we find consistent decreases in the best-fit y intercept with age for the substellar regime (as well as the stellar regime). Residuals of these age fits show a significant decrease in dispersion as a result of fitting the BD and stellar populations separately; the  $1\sigma$  standard deviation of the residuals for the BD population is 1.02 dex. We find a decrease of  $\sim$ 33% from the 1.36 dex found in Section 7.

In the substellar regime, we find higher accretion rates at the HBL compared to what is expected from the stellar best fit for each age. However, with the steeper slope, by the DBL, these

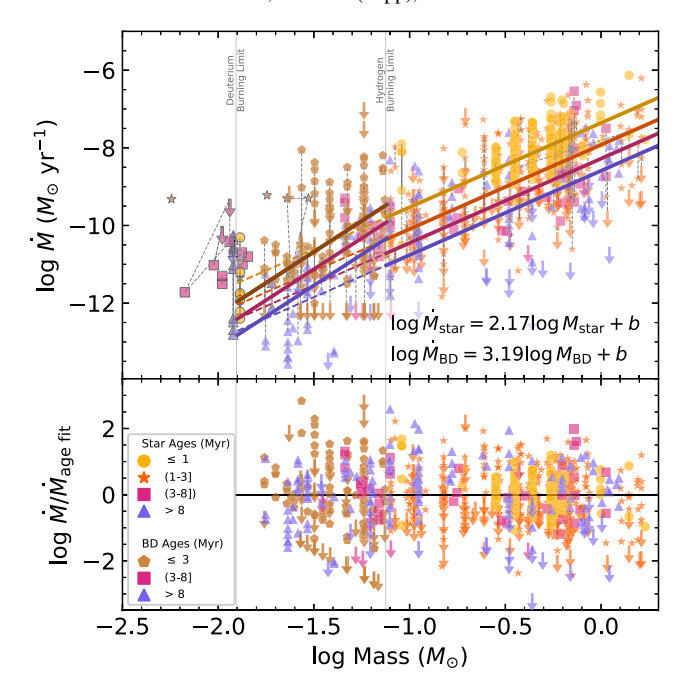


**Figure 16.** Top: CASPAR accretion rates vs. mass colored by age with best linear fits for each age and mass population (BDs and stars). We combined the BD  $\leq 1$  and (1-3] Myr populations to improve statistical number counts (brown pentagons). We extend the stellar fits into the BD regime indicated by the dashed lines. Bottom: residuals for the best linear fits for each age and mass population. The colors and markers are as in Figure 13.

relationships predict accretion rates just slightly lower than those extrapolated from the stellar best fits. Higher-mass BDs additionally appear to accrete faster at older ages compared to very-low-mass stars at similar ages, as seen at the HBL in Figure 16.

In order to access the rate of decay of accretion for the substellar population compared to the stellar population, we extract  $\log \dot{M}$  at the HBL and DBL for the stellar and substellar fits. We find the following exponential best fits to these data:

$$\dot{M}_{\rm stars} \propto 1.40e^{-t/3.0 \text{ Myr}},$$
 (7)

$$\dot{M}_{\rm BDs} \propto 1.35 e^{-t/5.2 \text{ Myr}},$$
 (8)

where  $\dot{M}$  is in  $M_{\odot}$  yr<sup>-1</sup>. We show these fits at the HBL and DBL as a function of binned age in Figure 17.

The exponential trend in the stellar regime is similar to the exponential disk fraction decay timescale ( $\tau$  = 2.5 Myr) found by Mamajek (2009), while the decay rate for BD accretion remains high compared to the  $\tau$  = 3 Myr timescale for disk fraction decay (Mamajek 2009), with objects still accreting quickly at older ages.

## 7.2. Relationship between Accretion Rate and Mass, Age, and Mass Population

To test whether the relations among mass accretion, object mass, and age show evolutionary trends that could explain the (lack of) knee in the accretion-rate timescale, we fit the  $\dot{M}-M$  relation with age (t) and mass as free parameters. More specifically, we fit the model

$$\log \dot{M} = \alpha M + \beta t + \gamma (\log M \times t) + \delta \tag{9}$$

for each mass population, where  $\dot{M}$  is in  $M_{\odot}$  yr<sup>-1</sup>, M in  $M_{\odot}$ , and t in Myr.

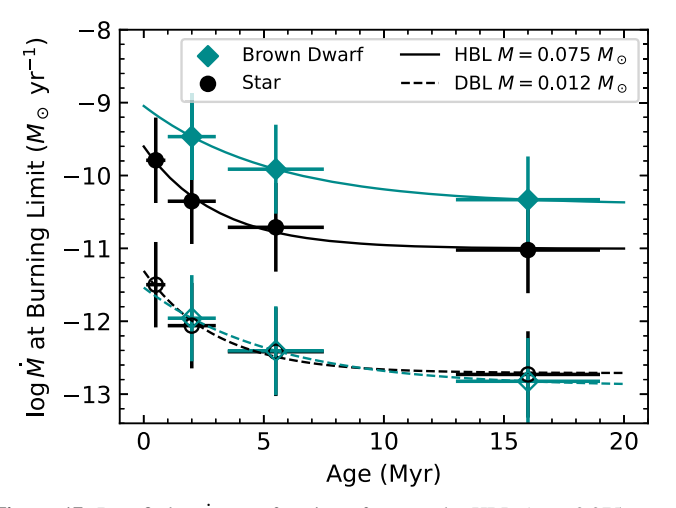


**Figure 17.** Best-fit  $\log \dot{M}$  as a function of age at the HBL  $(M=0.075\,M_\odot;$  solid line and filled markers) and at the DBL  $(M=0.012\,M_\odot;$  dashed line and open markers) for stars (black circles) and BDs (cyan diamonds) from Figure 16. We show the best exponential fits for each population and find that the BD accretion rates decrease at a faster rate compared to the stellar rates.

We find best-fit values for the stellar and BD populations, given by:

$$\log \dot{M}_{\text{star}} = 2.22(\pm 0.10) \log M_{\text{star}} - 0.14(\pm 0.01) t$$
$$-0.11(\pm 0.02) (\log M_{\text{star}} \times t) - 7.50(\pm 0.06)$$
(10)

and

$$\log \dot{M}_{\rm BD} = 1.28(\pm 0.60) \log M_{\rm BD} - 0.32(\pm 0.14)t$$
$$-0.31(\pm 0.09) (\log M_{\rm BD} \times t) - 8.29(\pm 0.81). \tag{11}$$

As shown in Figure 18, in the substellar regime, we find a clear mass and age dependence on accretion rate, with the slope increasing with age, while this trend flattens in the stellar regime. In older systems, we see a systematic steepening in the  $\dot{M}-M$  slope compared to the stellar regime. This is suggestive of a faster evolutionary timescale for accretion onto BDs (especially low-mass BDs), as they accrete material at a relatively higher rate ( $\dot{M} \sim 10^{-11}$ ) at young ages, depleting their disks quickly. Higher-mass BDs and stars instead accrete for longer at a high accretion rate ( $\dot{M} \sim 10^{-7}-10^{-10}$ ), indicative of relatively slower disk depletion at younger ages. This confirms previous work in individual SFRs showing a shallower substellar trend for younger systems (Manara et al. 2015; Fiorellino et al. 2021) and a steeper trend in older systems (Alcalá et al. 2017; Manara et al. 2017a).

When we fit to both mass and age, the standard deviation of the best-fit residuals for all objects is 0.78 dex, a 9% decrease from the single-population best-fit standard deviation (0.85 dex). Compared to the three population fits, the residual scatter decreases by 6% (0.71 dex from 0.75 dex) and 44% (0.94 dex from 1.36 dex) in the stellar and substellar regimes, respectively. When we remove the outlier upper limits, these decrease by 17%, 22%, and 58%, for the total, stellar, and BD populations, respectively, indicating both mass and age have a profound effect on the rate of accretion for BDs. This effect is also apparent when we bin by age (as discussed above) and have slope as a free parameter (see "By Age and Mass" in Table 4). For the stellar fits, the slope becomes shallower with age, while the BD fits become steeper. We also see this trend when we examine individual SFRs in Appendix F.

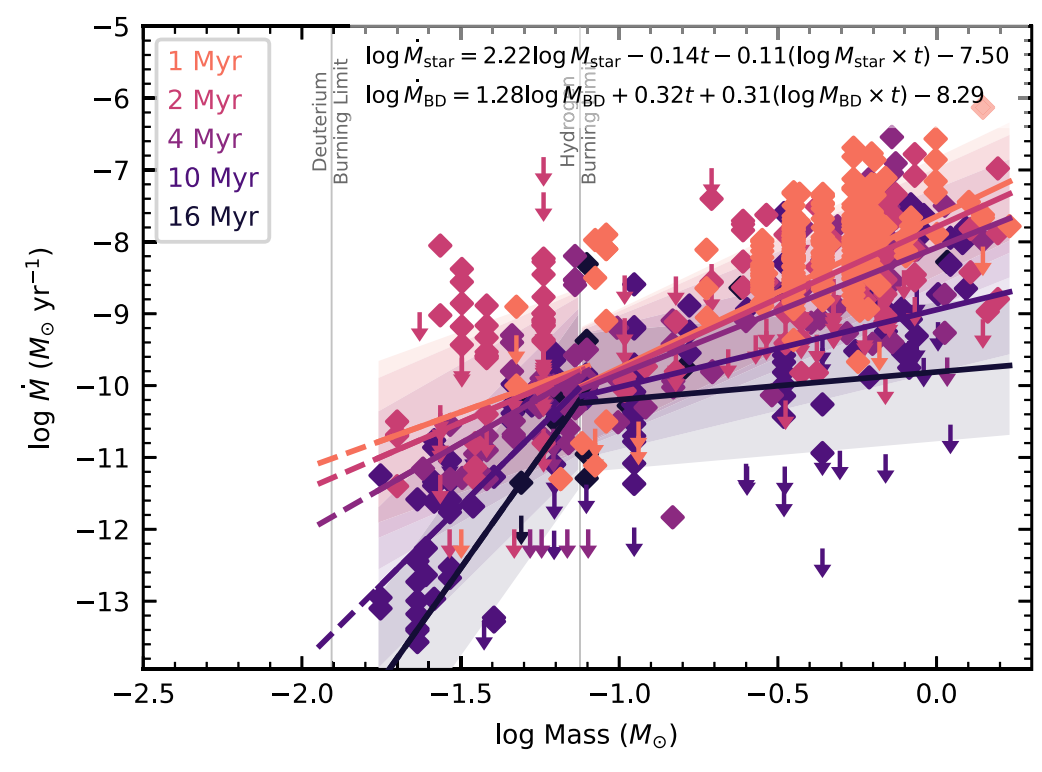


Figure 18. Accretion rate vs. mass for the star and BD populations colored by specific ages. The solid lines and bands show the best linear fits and  $1\sigma$  standard deviations, where age and mass are both free parameters for each mass population. The dashed lines are extrapolations to the DBL.

#### 8. Discussion

In Section 5.1, we find that uniformly deriving physical and accretion properties reduces the scatter in the CASPAR  $\dot{M}-M$  relation by 17%, indicating that methodology plays a role in the observed scatter when comparing accretion rates across multiple detection and analysis techniques. However, since a large ( $\sim$ 1 dex) scatter in the  $\dot{M}-M$  relationship has been seen even in surveys using one detection technique (e.g., Muzerolle et al. 2001; Herczeg & Hillenbrand 2008; Alcalá et al. 2017), methodology cannot fully explain the observed dispersion around the relation.

We first investigate the roles of accretion diagnostic, intrinsic variability, and age on the  $\dot{M}$ -M scatter. In the stellar regime, the scatter is consistent among diagnostics, especially between line luminosity and continuum excess. This is expected, as the  $L_{\rm acc}$ - $L_{\rm line}$  relationships are derived for young stellar objects (Rigliaco et al. 2011; Alcalá et al. 2014, 2017). We do start to see an increase in the line luminosity scatter in the substellar regime, with the median  $\dot{M}$  increasing  $\sim 0.8$  dex from the single-population  $\dot{M}$ -M relation (Figure 9), likely driven by NIR emission (Figure 10). Though we do see intrinsic accretion variability in  $\dot{M}$  over multiple lines at the same epoch or over multiple epochs ( $\sim$ 0.8 dex), as only 241 and 67 objects in CASPAR are contributing to this variability, respectively, they are likely not driving the scatter. Indeed, this spread is in line with previous surveys of accretion variability, and smaller than the total observed scatter (see Manara et al. 2023 and references therein). Finally, when we just consider age as a driving factor, we find that the  $\dot{M}$  scatter in each age bin is roughly the same as the overall scatter (see Figures 13 and 16) and normalizing by age has little effect.

Instead, we posit that the measured accretion rates, dispersion, and variability behavior of BDs are distinct from

the stellar regime. We find that three population fits (stars, BDs, and PMCs) are statistically favored over fits to a single population for objects of all masses and that fitting mass populations separately results in the greatest reduction in residuals. This is most clearly seen in the BD regime, where fitting for both mass and age reduces the residual scatter by 44%-58%. When the substellar and stellar populations are fitted separately, age effects are compensated for, and a uniform methodology is applied to derive accretion rates, the total scatter in the  $\dot{M}-M$  relation across all mass regimes decreases from 1.0 to 0.78 dex, a decrease of 28%.

The hypothesis of a different  $\dot{M}-M$  relation in the substellar regime is not unique to this work. Vorobyov & Basu (2009) predicted a bimodality in the  $\dot{M}-M$  relation; in particular, they predicted a steepening at lower masses. This  $\dot{M}-M$  bimodality was verified observationally by Alcalá et al. (2017) and Manara et al. (2017a) in the Chamaeleon I (1.5 Myr) and Lupus (2.5 Myr) regions, with a break at  $M \sim 0.2 \, M_{\odot}$ . However, this break was not seen in other regions of similar or younger ages (probing the stellar and high-mass substellar regimes; Manara et al. 2015; Fiorellino et al. 2021). Manara et al. (2023) suggest that it could be an evolutionary effect, wherein low-mass stars accrete their disk mass at a faster rate during the late stages of formation. From Figure 18, we see a similar trend, where the slope steepens with age for substellar masses, showing that this evolutionary effect is universal for BDs even in different SFRs.

Theoretical studies of BDs suggest a variety of formation mechanisms, from more planetary processes such as disk fragmentation (e.g., Bate et al. 2002, 2003) to protostellar embryo ejection (e.g., Goodwin et al. 2005; Hubber & Whitworth 2005) and turbulent fragmentation (e.g., Kirk et al. 2006). Previous observational surveys of BDs have found that their disk properties follow trends similar to stars,

with similar disk fractions (Luhman et al. 2005), correlations between disk and stellar mass (Testi et al. 2016; Ward-Duong et al. 2018; Rilinger & Espaillat 2021; Sanchis et al. 2021), and an inverse correlation between disk mass and age (Rilinger & Espaillat 2021). The lowest-mass BDs should have small disks; however, at the youngest ages, they appear to accrete material at similar rates to higher-mass BDs with larger disks (within an order of magnitude; see Figure 18). In other words, the slope of the  $\dot{M}-M$  relation for the youngest BDs is shallow. The steepening of the relation in  $\dot{M}-M$  with age could be a result of the lowest-mass BDs accreting "too rapidly" at younger ages and depleting their disk material.

Combining both physical and systematic offsets in the BD regime, evidence from CASPAR points to a twofold complication when deriving accretion rates for the lowest-mass objects. First, as discussed above, age and mass play a significant role in accretion rates (see Figure 18). Additionally, accretion rates derived from line luminosities are calculated using empirically derived  $L_{acc}$ - $L_{line}$  scaling relationships for stars. However, if stellar and substellar objects follow different  $\dot{M}$ -M relationships, there is no guarantee that the same  $L_{acc}$ - $L_{line}$  relationships accurately represent single (or bound) BDs. By using stellar relationships in the substellar regime, we could be artificially overestimating both the accretion luminosities and accretion rates derived from line luminosities. Systematic variations in accretion-rate scalings may play a role in the apparent variation among diagnostics for substellar objects, with up to a 0.8 dex difference in the inferred accretion rates for certain tracers (e.g., line fluxes versus excess continuum). Forthcoming work will explore this issue (S. K. Betti et al. 2023, in preparation), which may have a profound impact on the interpretation of substellar accretion.

## 8.1. PMC Population

In this section, we describe briefly the trends seen in the PMC population. Though the sample of accreting PMCs is small and has not been rederived consistently in mass or accretion rate, we note that these objects appear to follow a much flatter and higher relation compared to BDs. Stamatellos & Herczeg (2015) modeled the disk and accretion properties of bound companions formed via disk fragmentation, allowing a gravitationally unstable disk with a mass of 0.7  $M_{\odot}$  around a  $0.7~M_{\odot}$  star to grow until it started to fragment. They predict that the disks around PMCs are more massive than expected for objects of the same mass forming in isolation from a collapsing core. This is due to the fact that PMCs are forming within the larger circumstellar disk. Before they separate from the disk (become dynamically independent), they are able to accrete more gas than a BD whose only material reservoir is its natal core (Stamatellos & Herczeg 2015). Stamatellos & Herczeg (2015) predict no strong correlation between object mass and disk mass under this scenario, leading to a flatter slope in  $\dot{M}$ versus M.

The difference that we observe between high PMC accretion rates and low accretion rates for BDs of similar mass could be either: (a) an observational bias in observed PMCs, such that objects with accretion rates below  $10^{-12}\,M_\odot$  yr<sup>-1</sup> have simply gone undetected; (b) PMCs may be fundamentally different from BDs, for example, by forming via a disk-fragmentation-like mechanism as opposed to core collapse; or (c) using incorrect scaling relations pushes our  $\dot{M}$  estimates of all substellar objects up or increases the dispersion in the relation.

Recent theoretical work by Aoyama et al. (2018, 2020) and Marleau et al. (2022) also shows that bound PMCs may have a higher fraction of line emission contributing to their total accretion luminosity than accreting stars. These models predict significantly larger ( $\sim$ 2 dex) accretion rates for planetary mass objects than those derived from stellar magnetospheric empirical relations (Alcalá et al. 2014, 2017), which would drive these  $\dot{M}$ s to even higher rates. As BDs are traditionally used to place the accretion of PMCs in context, more care will have to be taken in calculating and interpreting accretion signatures from PMCs.

#### 9. Conclusion

In this paper, we introduce CASPAR, the Comprehensive Archive of Substellar and Planetary Accretion Rates—the largest database of substellar and planetary accretion rates to date. The physical and accretion properties in CASPAR have been rederived under a consistent methodology (Gaia distances, consistent evolutionary models, and scaling relations). The goal of this effort was to investigate the contribution of systematic offsets among methods to overall scatter in the  $\dot{M}-M$  relation. Using the rederived database, we investigate the dispersion in the  $\dot{M}-M$  relation, and the physical and systematic processes that contribute to it. We also explore variation among the star, BD, and planetary PMC populations. We find:

- 1. Rederiving all physical and accretion properties using the same methodology decreases the 1.04 dex of scatter about the single-population  $\dot{M}-M$  fit by 17%. The best single-population linear fit for CASPAR,  $\log \dot{M} = 2.02 \log M 8.02$ , is consistent with previous estimates from smaller samples, suggesting that methodological differences in derivation play a small role in the slope or scatter of the  $\dot{M}-M$  relation.
- 2. The choice of accretion diagnostic additionally contributes to the overall scatter at substellar masses, with estimates from line luminosities leading to an average of 0.8 dex variation for a single object. Within the stellar regime, accretion rates are consistent among tracers. Unlike line luminosity, excess-continuum-derived estimates are consistent to within 0.21 dex of the overall best linear fit across both the substellar- and stellar-mass regimes  $(0.1 \lesssim M/M_{\odot} \lesssim 2)$ .
- 3. We also find consistent multiepoch and multitracer variability of ~0.6 dex in the stellar regime, consistent with previous estimations. This variability increases to 1.33 dex in the substellar regime. We posit that this increase is due to either higher variability seen at lower masses or stellar scaling relations being invalid in substellar regimes, leading to offsets in the derived accretion rates.
- 4. We investigate the effect of age on dispersion around the relation and find a 1 dex decrease in the best-fit intercept between ∼1 and 10 Myr. However, the scatter within age bins is ∼1 dex, leading to little change in the overall scatter compared to the scatter from the overall best-fit residuals.
- 5. We argue that the majority of the scatter can be explained by modeling the star, BD, and PMC populations by separate  $\dot{M}$ –M relations, accounting for both mass and age. We find the BD  $\dot{M}$ –M scatter decreases by 44% as a

- result (58% when upper-limit outliers are excluded from the residuals). Additionally, we show that the BD  $\dot{M}-M$  relation steepens with age, while the stellar relation flattens.
- 6. We posit that there is a twofold issue when deriving accretion rates for low-mass objects. First, accretion rates are expected to depend much more on age and mass than in the stellar regime. Second, accretion rates derived from stellar scaling relations likely overestimate BD accretion rates, contributing to the overall scatter in this population.
- 7. Bound planetary companions seem to follow a flatter  $\dot{M}-M$  relation compared to BDs and stars. This may be a result of differences in either their formation or accretion paradigms. Accretion measurements for a larger population of PMCs and the individual modeling of these systems will help reveal the underlying physics governing them.

CASPAR is an evolving database and with future/ongoing surveys (e.g., Gangi et al. 2022; Pittman et al. 2022), protoplanet detections (e.g., Ringqvist et al. 2023), and derived scaling relations (e.g., Marleau & Aoyama 2022), it will continue to be updated. All updates and additions will be found on Zenodo: doi:10.5281/zenodo.8393053. Suggestions for additions to CASPAR can be made to the lead author.

## Acknowledgments

S.K.B. acknowledges support for this work from the NASA Future Investigators in NASA Earth and Space Science and Technology grant 80NSSC22K1750 (FI: S. K. Betti; PI: D.

Calzetti, co-I: K. Follette). K.B.F. acknowledge funding from NSF-AST-2009816 and the Cottrell Scholar Award #28290. G.-D.M. acknowledges the support of the DFG priority program SPP 1992 "Exploring the Diversity of Extrasolar Planets" (MA 9185/1) and from the Swiss National Science Foundation under grant 200021\_204847 "Planets In Time." This work has made use of data from the European Space Agency (ESA) mission Gaia (https://www.cosmos.esa.int/ gaia), processed by the Gaia Data Processing and Analysis Consortium (DPAC; https://www.cosmos.esa.int/web/gaia/ dpac/consortium). Funding for the DPAC has been provided by national institutions, in particular the institutions participating in the Gaia Multilateral Agreement. This research has made use of the SIMBAD database, operated at CDS, Strasbourg, France. This research has made use of the VizieR catalog access tool, CDS, Strasbourg, France (doi: 10.26093/cds/ vizier). The original description of the VizieR service was published in 2000, A&AS 143, 23. Parts of this work have been carried out within the framework of the NCCR PlanetS supported by the Swiss National Science Foundation.

Software: astropy (Astropy Collaboration et al. 2013, 2018), Matplotlib (Hunter 2007), numpy (Harris et al. 2020), astroquery (Ginsburg et al. 2019), scipy (Virtanen et al. 2020).

## Appendix A CASPAR Column Names

In Table 6, we give all columns within the database and their description. These are identical between the Literature Database and CASPAR.

 Table 6

 Contents of CASPAR and Literature Database

Contents of CASPAR and Literature Database			
Column Label	Description, Comment, and/or Units		
Unique ID	CASPAR source ID		
Unique Name	2MASS Point Source Catalog or common name ID		
Simbad-Resolvable Name	ID resolvable with Simbad		
Reference Name	Source ID used by reference		
Duplicate #	# for duplicate object		
Total Duplicates	# of duplicate objects		
Binary	Binary flag		
Companion	Flag on companion		
Separation	Separation of binary or companion (arcsec)		
Object	Type of object (star/BD/PMC)		
R.A. (J2000.0)	Right ascension J2000 (deg)		
Decl. (J2000.0)	decl. J2000 (deg)		
R.A. (J2016.0)	Gaia right ascension J2016 (deg)		
Decl. (J2016.0)	Gaia decl. J2016 (deg)		
Disk Type	Disk class		
Association	SFR or association		
Association Probability Banyan Sigma	Banyan $\Sigma$ association probability (Gagné et al. 2018)		
Association Census Reference	Association census reference object is in		
Association Age	Age of association from isochrone fitting (Myr)		
Association Age err	Uncertainty on association age (Myr)		
Individual Age	Individual object age (Myr)		
Individual Age err	Individual object age uncertainty (Myr)		
Individual Age Reference	Reference for individual age		
GAIA DR2 Source ID	reference for marvidua age		
GAIA DR2 Parallax	(mas)		
GAIA DR2 Parallax err	(mas)		
GAIA DR2 Reliable Parallax	Parallax reliability flag		
GAIA DR2 Distance	From Bailer-Jones et al. (2018; pc)		
GAIA DR2 Distance lower limit	From Bailer-Jones et al. (2018; pc)		
GAIA DR2 Distance upper limit	From Bailer-Jones et al. (2018; pc)		
GAIA DR2 RA proper motion	(mas $yr^{-1}$ )		
GAIA DR2 RA proper motion err	$(\text{mas yr}^{-1})$		
GAIA DR2 Dec proper motion	$(\text{mas yr})$ $(\text{mas yr}^{-1})$		
GAIA DR2 Dec proper motion err	$(\text{mas yr})$ $(\text{mas yr}^{-1})$		
GAIA EDR3 Source ID	(mas yr )		
GAIA EDR3 Soulce ID  GAIA EDR3 Parallax	(mas)		
GAIA EDR3 Parallax err	(mas)		
GAIA EDR3 Reliable Parallax	Parallax reliability flag		
GAIA EDR3 Geometric Distance	From Bailer-Jones et al. (2021; pc)		
GAIA EDR3 Geometric Distance lower limit	From Bailer-Jones et al. (2021; pc)		
GAIA EDR3 Geometric Distance upper limit	From Bailer-Jones et al. (2021; pc)		
GAIA EDR3 RA proper motion	(mas yr <sup>-1</sup> )		
GAIA EDR3 RA proper motion err	(mas yr <sup>-1</sup> )		
GAIA EDR3 Dec proper motion	(mas yr <sup>-1</sup> )		
GAIA EDR3 Dec proper motion err	(mas yr <sup>-1</sup> )		
	(mas yr) $(\text{km s}^{-1})$		
radial velocity (barycentric)	$(\text{km s}^{-1})$		
radial velocity err (barycentric)			
A_V	Visual extinction (mag)		
A_V err	Visual extinction uncertainty (mag)		
A_J	J-band extinction (mag)		
A_J err	J-band extinction uncertainty (mag)		
A_V reference	Visual extinction reference		
Jmag	J apparent magnitude (mag)		
Jmag err	J apparent magnitude uncertainty (mag)		
Hmag	H apparent magnitude (mag)		
Hmag err	H apparent magnitude uncertainty(mag)		
Kmag	K apparent magnitude (mag)		
Kmag err	K apparent magnitude uncertainty (mag)		
Ha mag	$H\alpha$ apparent magnitude (mag)		
Ha mag err	$H\alpha$ apparent magnitude uncertainty (mag)		
Reference	Original literature source for accretion-rate measurement		
Telescope/Instrument	Facility used to measure accretion rate		
Association	Association/SFR used by CASPAR		

Table 6 (Continued)

Column Label	Description Commant and/or Units
-	Description, Comment, and/or Units
Age	CASPAR age (Myr)
Age err	Average CASPAR age uncertainty (Myr)
Epoch	Epoch of original accretion-rate tracer observation
$\log g$	Surface gravity
Distance	CASPAR distance (pc)
Distance err lower limit	CASPAR distance lower sigma (pc)
Distance err upper limit	CASPAR distance upper sigma (pc)
Sp Type	Spectral type
Sp Type err	Spectral type uncertainty
Teff	Effective temperature (K)
Teff err	Effective temperature uncertainty (K)
Mass	$(M_{\odot})$
Mass err	$(M_{\odot})$
Luminosity	$(L_{\odot})$
Luminosity Err	$(L_{\odot})$
Radius	$(R_{\odot})$
Radius err	$(R_{\odot})$
Accretion Diagnostic	Method to derive $\dot{M}$
Tracer	Lines or continuum
m Hlpha~10%~Upper~Limit	Upper-limit flag on $\dot{M}$
$H\alpha$ 10%	$(\text{km s}^{-1})$
$H\alpha$ 10% err	$(\text{km s}^{-1})$
$H\alpha$ 10% Accretion Rate	$\dot{M}$ derived from H $\alpha$ 10%
Line <sup>a</sup> Upper Limit	Upper-limit flag on $\dot{M}$ for line
Line <sup>a</sup> EW	Equivalent width for line (Å)
Line <sup>a</sup> EW err	Equivalent width uncertainty for line (Å)
Line <sup>a</sup> Line Flux	Line flux for line (erg s <sup>-1</sup> cm <sup>-2</sup> )
Line <sup>a</sup> Line Flux err	Line flux uncertainty for line (erg s <sup>-1</sup> cm <sup>-2</sup> )
Line Log Accretion Luminosity	Accretion luminosity scaled from line ( $L_{\odot}$ )
Line Log Accretion Luminosity err	Accretion luminosity scaled from line $(L_{\odot})$ Accretion luminosity uncertainty scaled from line $(L_{\odot})$
Line <sup>a</sup> Accretion Rate	Accretion rate for line $(M_{\odot} \text{ yr}^{-1})$
Line Accretion Rate err	Accretion rate for line $(M_{\odot} \text{ yr}^{-1})$ Accretion-rate uncertainty for line $(M_{\odot} \text{ yr}^{-1})$
	Flag on $\dot{M}$ upper limit
Upper Limit	* **
Log Accretion Luminosity	Accretion luminosity from accretion diagnostic $(L_{\odot})$
Log Accretion Luminosity err	Accretion luminosity uncertainty from accretion diagnostic ( $L_{\odot}$
Accretion Rate	Accretion rate from accretion diagnostic $(M_{\odot} \text{ yr}^{-1})$
Accretion Rate err	Accretion-rate uncertainty from accretion diagnostic $(M_{\odot} \text{ yr}^{-1})$
Scaling Relation	$L_{\text{line}} - L_{\text{acc}}$ scaling relation reference
SpTemp Conversion	Spectral type-to-temperature conversion reference
Evolutionary Models	Evolutionary model method
Notes	
Links	Link to SIMBAD

Notes. Only a portion of this table is shown here to demonstrate its form and content. Machine-readable versions of CASPAR (Part 1) and the Literature Database (Part 2) are available.

a Lines: Hα, Hβ, Hγ, Hδ, Hε, H8, H9, H10, H11, H12, H13, H14, H15, Paβ, Paγ, Paδ, Pa8, Pa9, Pa10, Brγ, Br8 Pfβ, He I  $\lambda$  4026, He I  $\lambda$  4471, He I  $\lambda$  4713, He I  $\lambda$  5016, He I  $\lambda$  5876, He I  $\lambda$  6678, He I  $\lambda$  7065, He I  $\lambda$  10830, He II  $\lambda$  4686, Ca II K, Ca II H, Ca II  $\lambda$  8498, Ca II  $\lambda$  8542, Ca II  $\lambda$  8662, Na I  $\lambda$  5889, Na I  $\lambda$  5896, O I  $\lambda$  8446, and C IV  $\lambda$  1549.

(This table is available in its entirety in machine-readable form.)

## Appendix B Literature Database Compilation

#### B.1. Kinematic, Photometry, and Age Information

For each object, we compiled kinematic information (R.A., decl., parallax, distance, proper motion, and radial velocity) from Gaia DR2 (Gaia Collaboration et al. 2016, 2018) and Gaia EDR3 (Gaia Collaboration et al. 2016, 2021), in case an object was not observed in one of the data releases. We queried the Gaia archives in order to find the Gaia object associated with each database entry. Of the 793 unique objects, we retrieved kinematic information for 670 that have Gaia observations (of

the substellar objects, 65/87 have Gaia observations). If the parallax is considered reliable (e.g., its parallax error is less than 25% and parallax >0.167 mas; Huang et al. 2022), we use the geometric distances found for DR2 and EDR3 by Bailer-Jones et al. (2018) and Bailer-Jones et al. (2021), respectively. NIR photometry for each object is compiled from the Two Micron All Sky Survey (2MASS), while the accretion literature reference  $H\alpha$  photometry is included for objects whose accretion rates are measured from this photometry.

For objects with D <150 pc, we ran their kinematic information through the Banyan  $\Sigma$  tool (Gagné et al. 2018) in order to determine the most likely host association. If the

Table 7
SFRs and Association Ages and Distances

Region	# in CASPAR	Age	Age	Distance	Distance
		(Myr)	References	(pc)	References
25 Orionis	1	$6.2 \pm 2.3$	1	$354 \pm 3$	1
118 Tau	1	10	2		
Argus	1	$45 \pm 5$	3		
$\beta$ Pictoris	1	$24 \pm 3$	4	$40 \pm 17$	5
Chamaeleon I North	57	$1.5 \pm 0.5$	6	$191\pm0.8$	6
Chamaeleon I South	47	$1.5 \pm 0.5$	6	$187 \pm 1$	6
Corona-Australis	3	$1.5 \pm 0.5$	7		
$\eta$ Chamaeleontis	15	$11 \pm 3$	4	94	8
IC 348	8	$4\pm2$	9	$321\pm10$	10
Lagoon Nebula	224	$0.7 \pm 0.4$	11	$1326^{+77}_{-69}$	12
Lupus	19	$2.6 \pm 0.5$	13, 14	$158\pm0.6$	13
Lupus 1	3	$1.2 \pm 0.6$	13	$155^{+3.2}_{-3.4}$	13
Lupus 2	5	$2.6 \pm 0.5$	13	$158^{+7}_{-5}$	13
Lupus 3	34	$2.5 \pm 0.5$	13	$159 \pm 0.7$	13
Lupus 4	7	$2.4 \pm 1.3$	13	$160 \pm 1$	13
NGC 2024	1	$1.1\pm1$	1		
$\rho$ Oph	26	~6	15	140	15
ρ Oph/L1688	76	$2\pm1.2$	15	138	15
$\sigma$ Ori	89	$1.9 \pm 1.6$	1	$406 \pm 4$	1
Sh 2-284	3	$3.5 \pm 1$	16	4000	16
Taurus	12	$2\pm1$	17	140	17
Taurus/B213	2	$3.1 \pm 0.9$	17	156	17
Taurus/L1495	13	$1.3 \pm 0.2$	17	130	17
Taurus/L1517-Center	6	$2.5 \pm 1$	17	155	17
Taurus/L1517-Halo	1	$2.3 \pm 0.5$	17	157	17
Taurus/L1524	15	$1.6 \pm 0.9$	17	128	17
Taurus/L1527	5	$2.6 \pm 0.8$	17	142	17
Taurus/L1544	1	$3.4 \pm 0.9$	17	168	17
Taurus/L1546	5	$2\pm0.3$	17	160	17
Taurus/L1551	8	$1.7 \pm 0.2$	17	145	17
Taurus/L1558	3	$3.3 \pm 0.4$	17	147	17
Taurus/North	5	$2.5 \pm 0.4$	17	143	17
Taurus/South	1	$6.2 \pm 1.7$	17	123	17
Tucana–Horologium	1	$45 \pm 4$	4		
TW Hydra	13	$10 \pm 3$	4	50	18
Upper Centaurus Lupus	15	$16\pm 2$	19	$130^{+62}_{-32}$	19
Upper Scorpius	68	$10 \pm 3$	14, 19, 20	$141^{+77}_{-37}$	19
Opper Scorpius	00	10 ± 3	17, 17, 20	171_37	1)

Note. References: (1) Kounkel et al. (2018); (2) Gagné et al. (2018); (3) Zuckerman (2019); (4) Bell et al. (2015); (5) Messina et al. (2017); (6) Galli et al. (2021); (7) Esplin & Luhman (2022); (8) van Leeuwen (2007); (9) Bell et al. (2013); (10) OrtizLeón et al. (2018); (11) Prisinzano et al. (2019); (12) Wright et al. (2019); (13) Galli et al. (2020); (14) Luhman (2020); (15) Esplin & Luhman (2020); (16) Kalari & Vink (2015); (17) Krolikowski et al. (2021); (18) Schneider et al. (2016); (19) Pecaut & Mamajek (2016); (20) Ratzenböck et al. (2023).

membership probability is >70%, we assume membership in that association and assign the object the corresponding age from Table 7. For those objects D >150 pc or whose membership probabilities were lower than 70%, we searched the literature for population census studies that may have determined the membership in an association or a cluster. Finally, for those objects not in Banyan  $\Sigma$  or census papers, we determine if (a) it is a known field star, or (b) if its kinematic information is close to an association. If the latter, we assign it to the closest association, with the caveat that the association is only assumed, indicated by a "\*" next to the assigned association in the database.

In order to estimate object ages, we compile a list of the SFRs, clusters, associations, and clouds associated with each object. Star formation is not instantaneous within molecular clouds, but occurs on individual, subgroup, and regional levels, leading to gradients and even separate age populations within

these associations. Additionally, effects such as extinction, accretion history, and binarity affect the observational uncertainty when determining ages (Krolikowski et al. 2021). These can lead to vertical scatter on Hertzsprung–Russell diagrams (HRDs; Baraffe et al. 2017), a result of the variation in the radius-to-mass ratio driven primarily by variations such as age (Pecaut et al. 2012; Soderblom et al. 2014; Rizzuto et al. 2016). These large uncertainties make individual age estimates hard to derive from HRDs and rife with large uncertainties (Pecaut et al. 2012; Malo et al. 2014; Feiden 2016; Rizzuto et al. 2020). Additionally, other methods of calculating ages (i.e., lithium burning and kinematics) all have intrinsic assumptions and systematic effects on the error (see Soderblom et al. 2014 for a detailed review of these effects).

Therefore, recent studies of SFRs have relied on robustly estimating the ages of the groups within SFRs, which reduces the vertical spread resulting from assuming a single age, as well

**Table 8**Literature References

Reference	Accretion Diagnostic	Tracer(s) or Spectra Wavelength Range
Alcalá et al. (2014)	Continuum Excess	≈3400–3600, ≈4000–4750, 3600, 4600, 7100 Å
Alcalá et al. (2017)	Continuum Excess	≈3400–3600, ≈4000–4750, 3600, 4600, 7100 Å
Alcalá et al. (2019)	Line Luminosity	C IV λ 1549
Alcalá et al. (2020)	Continuum Excess	≈3400–3600, ≈4000–4750, 3600, 4600, 7100 Å
Alcalá et al. (2021)	Line Luminosity	$H\alpha$ , $H\beta$ , $H\gamma$ , $H\delta$ , $Pa\beta$ , $Pa\gamma$ , $Pa\delta$ , $Pa\epsilon$ ,
		Ca I $\lambda$ 3934, He I $\lambda$ 4026, $\lambda$ 4471, $\lambda$ 4713, $\lambda$ 4922,
		He I $\lambda$ 5016, $\lambda$ 5876, $\lambda$ 6679, $\lambda$ 10830
Betti et al. (2022)	Line Luminosity	Pa $\gamma$ , Pa $\beta$ , Br $\gamma$
Bowler et al. (2011)	Line Luminosity	$\mathrm{Pa}\beta$
Calvet & Gullbring (1998)		
Close et al. (2014)	Line Luminosity	$H\alpha$ photometry
Comerón et al. (2010)	Line Luminosity	Са ІІ
Eriksson et al. (2020)	Line Luminosity	$H\alpha$ 10% width, $H\alpha$ , $H\beta$ , He I $\lambda$ 6678
Espaillat et al. (2008)	Line Profile	$_{ m Hlpha}$
Gatti et al. (2006)	Line Luminosity	$\mathrm{Pa}\beta$
Gatti et al. (2008)	Line Luminosity	$\mathrm{Pa}\gamma$
Gullbring et al. (1998),	Continuum Excess	3200–5400 Å
Haffert et al. (2019)	Line Profile	$H\alpha$ 10% width
Hashimoto et al. (2020)	Line Luminosity	$H\alpha, H\beta$
Herczeg & Hillenbrand (2008)	Continuum Excess	3200–9000 Å
Herczeg et al. (2009)	Continuum Excess	3200–9000 Å
Ingleby et al. (2013)	Continuum Excess	1570–7000 Å
Kalari & Vink (2015)	Line Luminosity	$H\alpha$ photometry
Kalari et al. (2015)	Line Luminosity	$H\alpha$ photometry
Lee et al. (2020)	Line Profile	$H\alpha$ 10% width
Manara et al. (2015)	Line Luminosity	Са п
Manara et al. (2016a)	Continuum Excess	3300–7100 Å
Manara et al. (2017b)	Continuum Excess	3300–7150 Å
Manara et al. (2020)	Continuum Excess	3300–7100 Å
Manara et al. (2021)	Line Luminosity	$H\alpha$ , $H\beta$ , He I $\lambda$ 5876, O I $\lambda$ 6300
Mohanty et al. (2005)	Line Luminosity	Са ІІ
Muzerolle et al. (2003)	Line Profile, Continuum Excess	$H\alpha$ , 5500, 6200, 6450, 7100, 8700, 8900 Å
Muzerolle et al. (2005)	Line Profile	m Hlpha
Natta et al. (2004)	Line Profile, Line Luminosity	$H\alpha$ , $Pa\beta$
Natta et al. (2006)	Line Luminosity	$Pa\beta$ , $Br\gamma$
Nguyen-Thanh et al. (2020)	Line Profile	$H\alpha$ 10% width
Petrus et al. (2020)	Line Luminosity, Line Profile	$H\alpha$ , $H\alpha$ 10% width
Pouilly et al. (2020)	Line Luminosity	$H\alpha$ , $H\beta$ , Ca II $\lambda$ 8542, $\lambda$ 8662
Rigliaco et al. (2011)	Continuum Excess, Line Profile	<i>U</i> -band photometric excess, H $\alpha$ 10% width
Rigliaco et al. (2012)	Continuum Excess	3000–25,000 Å
Rugel et al. (2018)	Continuum Excess	3000–5500 Å
Sallum et al. (2015)	Line Luminosity	$H\alpha$ photometry
Salyk et al. (2013)	Line Luminosity	${ m Pf}eta$
Santamaría-Miranda et al. (2018)	Line Luminosity, Line Profile	$H\alpha$ , H 11, Ca II line flux, $H\alpha$ 10% width
Venuti et al. (2019)	Continuum Excess,	≈3400–3600, ≈4000–4750, 3600, 4600, 7100 Å
(/	Line Luminosity	$H\alpha$ , $H\beta$ , $H\gamma$ , $H\delta$ , $H$ 8, $H$ 9, $H$ 10, $H$ 11,
		Pa $\beta$ , Ca II $\lambda$ 3934, He I $\lambda$ 4026, $\lambda$ 5876
Wagner et al. (2018)	Line Luminosity	$H\alpha$ photometry
White & Basri (2003)	Continuum Excess	6500 Å
Wu et al. (2015)	Line Luminosity	$H\alpha$ photometry
Wu et al. (2017)	Line Luminosity	$H\alpha$ photometry
Zhou et al. (2014)	Continuum Excess	3365 Å photometry

as the large uncertainty from assuming individual ages (e.g., Esplin & Luhman 2020; Galli et al. 2020, 2021; Krolikowski et al. 2021). This method relies on placing objects on an HRD and comparing to known isochrone and evolutionary track models to estimate age and mass, respectively. Though there are systematic and observational uncertainties due to potential differences in the models used and assumptions of temperature and luminosity, this method has been employed previously for all of the associations found in CASPAR, providing a (semi-)

uniform method to derive ages. We investigate if assuming a single age for the whole SFR affects the resulting masses and accretion rates (and the effect on the  $\dot{M}$ –M scatter). Using Taurus, as there is a large number of subregions and ages, we compare the radius-to-mass ratio derived from assuming a single age (2  $\pm$  1 Myr) and ages from the separate regions (see Table 7). We find that assuming a single age for a whole SFR only affects the radius-to-mass ratio and accretion rate by less than <20% compared to using region ages. This is generally

less than the uncertainty on both the individual and SFR ages  $(\sim 50\%)$  and likely does not greatly affect the derived accretion rates. We therefore use the average age from the most recent census papers for each region (see Table 7) corresponding to the (sub)cluster/association of which the object is a member. Individual object ages estimated from isochrone fitting from the literature reference are also included in the database.

#### B.2. Literature Database

For each accretion rate, we compile the literature reference and the physical and accretion properties used to calculate  $\dot{M}$ . This includes the association, age, and distance specific to the literature reference, as well as the spectral type, mass, luminosity, and radius. If any quantity is not specified in its reference, it is left blank. We also record, if given, the reference used to convert from spectral type to temperature, the evolutionary model used to derive estimates of physical parameters, and the emission-line luminosity to accretion luminosity  $(L_{line} - L_{acc})$  scaling relation. For each accretion rate, we list the specific accretion signature or continuum band used to calculate  $\dot{M}$ . We list the main accretion diagnostic for each reference in Table 8. We also compile all individual lineemission quantities (equivalent widths, line fluxes, accretion luminosities, and accretion rates) reported in the paper. In cases where the accretion rate is not presented in the reference, but can be calculated, we have done so and included them in the database. Finally, the accretion luminosity and rate found from the main reported literature reference are recorded. Objects with multiple measurements (from multiple studies, tracers, or epochs) are connected with a gray dashed line and highlight the variations in published estimates of mass and mass accretion rate across multiple studies and accretion diagnostics.

## Appendix C Unified Rederivation of Parameters

## C.1. Physical Parameters

Below we describe the unified methodology used to determine the physical parameters for each object in CASPAR, focusing exclusively on the stars and BDs.

Distance. We assume Gaia EDR3 distances for all objects with measurements in that data release (N=599; Bailer-Jones et al. 2021). If an object was not observed with EDR3, we use its Gaia DR2 distance (N=5; Bailer-Jones et al. 2018). If the object had no Gaia measurement, we assume the average distance to the region listed in Table 7 (N=189 in Appendix B). The uncertainty on each Gaia distance is from either Bailer-Jones et al. (2018) or Bailer-Jones et al. (2021), who estimate the  $1\sigma$  span of the highest-density interval on the posterior probability density used to determine the distance. This  $1\sigma$  span sets the lower and upper bounds of the distance and is not assumed to be symmetric around the median distance.

Age. We assume the age and uncertainty of the SFR or association as described in Appendix B.1. We refer to the individual papers for full details of the age and uncertainty determination.

Spectral Type. For objects that have only one measured accretion rate in the literature database (N=646), we assume the literature reference spectral type. For objects with multiple measured accretion rates (N=152), we assume the most recently measured spectral type. For objects with no spectral

types listed in their reference paper, we searched VizieR (Ochsenbein et al. 2000) and SIMBAD (Wenger et al. 2000) for a spectral type. If none was found, but a temperature was given, we either (a) calculated the spectral type using the spectral type-to-temperature conversion if stated in the literature reference, or (b) calculated the spectral type using the spectral type-to-temperature conversions of Herczeg & Hillenbrand (2014), if there was none stated. For spectral types without listed uncertainties, we adopt the spectral class uncertainty of Herczeg & Hillenbrand (2014): M dwarfs: 0.2 subclass; K8–M0.5: 0.5 subclass; and G0–K8: 1 subclass.

Effective Temperature. Temperature is calculated using the spectral type-to-temperature conversion of Herczeg & Hillenbrand (2014). The uncertainty is found by calculating the temperature at the upper and lower limits of the spectral type estimate. We then take the average value of the difference between the bounds and the given temperature as the uncertainty.

Mass, Luminosity, Radius, and Surface Gravity. To consistently estimate mass, luminosity, and radius, we use the evolutionary models of Baraffe et al. (2015) and the MIST MESA models (Paxton et al. 2011, 2013, 2015; Choi et al. 2016; Dotter 2016). Using the object age and temperature, we interpolate over the isochronal models to determine the mass, luminosity, radius, and surface gravity. We heavily modified the isochrone 19 Python package (Morton 2015) to work with the Baraffe et al. (2015) models and to interpolate between temperatures (the package currently only interpolates between masses). After interpolating over age and effective temperature, the best-fit mass, luminosity, radius, and surface gravity can be extracted. To determine the uncertainty on these quantities, we find the lower and upper limits on the age and temperature; this produces four bounds (1: low age/low temperature; 2: low age/high temperature; 3: high age/low temperature; and 4: high age/high temperature). We then take the average of the difference between the bound values and the given value as the uncertainty. We assume that all reported spectral types and line luminosities have been corrected for extinction.

#### C.2. Accretion Parameters

Below we detail the unified methodology used to derive accretion rates for various accretion diagnostics.

Continuum Excess. Accretion luminosities are determined from the total excess luminosity (derived from spectral template fitting), which has traditionally been assumed to result primarily from the continuum excess. From Herczeg & Hillenbrand (2008),  $L_{\rm acc} \propto d^2$ . Therefore, using the original literature accretion luminosities, we scale them by the Gaia distances and then derive an accretion rate using the updated accretion luminosity, mass, and radius.

Line Luminosities. For papers that report line fluxes (excluding the Mohanty et al. 2005 Ca II  $\lambda$  8662 line; see below), we calculate mass accretion rates from the reported line flux under a single set of scaling relations. For references that only report the accretion luminosity or accretion rate of the line (s), we use the  $L_{\rm line}-L_{\rm acc}$  scaling relations and distance given in the paper to infer the measured line flux. For studies that only give accretion rates, we first calculate  $L_{\rm acc}$  using the reference mass and radius and then proceed as above. Once we

<sup>19</sup> https://github.com/timothydmorton/isochrones

have derived a line flux, we calculate the accretion rate as follows:

- 1. We update the line luminosity using the Gaia DR2 or EDR3 distance and assuming isotropic emission:  $L_{\text{line}} = 4\pi d^2 F_{\text{line}}$ .
- 2. We convert the line luminosity to accretion luminosity following  $\log(L_{\rm acc}/L_{\odot}) = a \times \log(L_{\rm line}/L_{\odot}) + b$ , using a single set of independently derived scaling relations (those of Salyk et al. 2013; Alcalá et al. 2017).
- 3. We convert to the accretion rate using our rederived mass and radius with Equation (1).

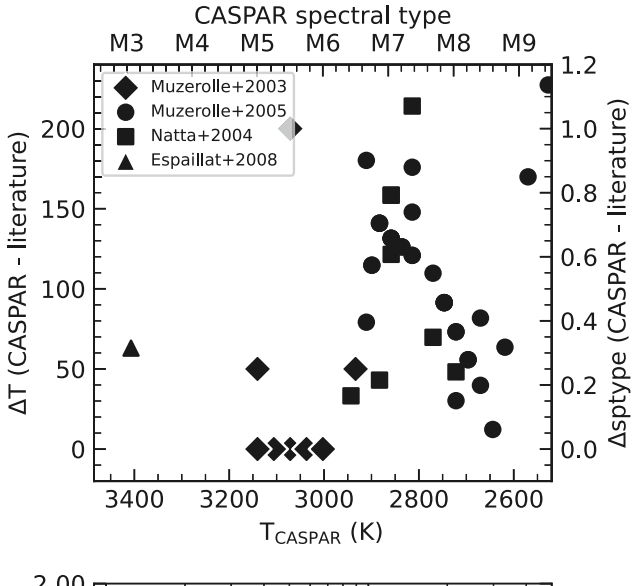
For objects with given line flux uncertainties, we propagate this error forward using the uncertainties on Gaia distance, rederived mass, and radius uncertainties, and the uncertainties on the scaling relationship.

The Ca II 8662 Å line fluxes calculated by Mohanty et al. (2005) are a unique case, as the line fluxes are calculated assuming a best-fit modeled continuum, causing systematic offsets between their values and the "true" values (for full details, see Mohanty et al. 2005). Therefore, we use their scaling relations (their Equations 1 and 3) in step 2 above.

 $H\alpha$  photometric Luminosities. Narrowband  $H\alpha$  photometry has frequently been used to calculate mass accretion rates for substellar objects (e.g., Close et al. 2014; Kalari et al. 2015; Sallum et al. 2015; Wu et al. 2015, 2017; Wagner et al. 2018). Once the  $H\alpha$  luminosity is determined, an  $L_{H\alpha}-L_{acc}$  scaling relation can be applied. Therefore, in order to recalculate the accretion rate, we follow the same procedure as for our rederivation of spectroscopic line fluxes (see above), substituting recalculated physical parameters (distance, mass, and radius) and adopting a single scaling relation (Alcalá et al. 2017).

However, for 16 objects in the Kalari et al. (2015) Lagoon Nebula sample ( $D \sim 1326$  pc), Gaia EDR3 distances put them at  $\sim 200$ –700 pc. Henderson & Stassun (2012) proposed that the cluster might be 15% closer than previous estimates; however, even with a closer distance, these objects are still well below any assumed distance to the cluster. Additionally, 10 of the objects have proper motions with R.A. and decl. dispersion greater than the best-fit values found for the Lagoon Nebula ( $\sigma_{\mu_{\alpha}} \sim 4.06$  km s  $^{-1}$ ,  $\sigma_{\mu_{\delta}} \sim 2.8$  km s  $^{-1}$ ; Wright et al. 2019), assuming a distance of 1326 pc. Therefore, we assume these objects are not true members of the Lagoon Nebula, and their true ages are unknown. Therefore, their masses cannot be estimated properly and we exclude them from further analysis.

*Line Profiles.* Accretion rates found by modeling the H $\alpha$ emission profile with radiative transfer models of the magnetosphere rely on the line-of-sight inclination angle of the disk and velocity field. Gas velocities are sensitive to mass (Muzerolle et al. 2001). Though the input mass range will vary according to the evolutionary tracks used, the best-fit model diverges if the mass is varied by a factor of 2 or more (due to significant variation in the model gas velocity;  $v_{\rm gas} \propto \sqrt{M}$ ). For object radii, uncertainty results from the spectral type-temperature conversion, with a 200 K error (equivalent to one spectral subclass) equal to 30% error in radius. Nonetheless, as the modeled gas density is not strongly dependent on radius (it depends on the system geometry), the model is less sensitive to variation. Therefore, as long as the rederived masses are approximately within a factor of 2, the temperatures are within 200 K (one spectral subclass), and/or the radii are within 30%



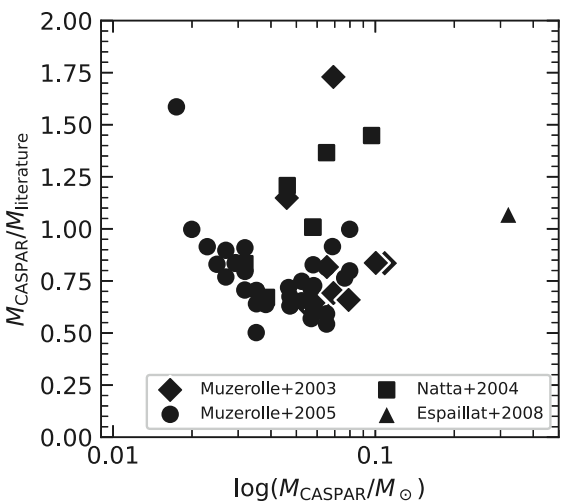


Figure 19. Absolute difference between the literature and CASPAR-derived temperatures/spectral types as a function of CASPAR temperature/spectral type (top) and the ratio between the literature and CASPAR-derived masses as a function of CASPAR mass (bottom) for objects with accretion rates derived from  $H\alpha$  emission profile modeling. The estimated accretion rates do not vary with rederived masses and radii if the spectral types are within one subclass (<200 K difference) and masses are within a factor of 2 of the original values. We find all values in CASPAR to be within those parameters.

of the literature values, no rederivation is needed. From Figure 19, we find that the average difference in temperature is 94 K (corresponding to half a spectral class) and the masses are within a factor of 0.83, and therefore the accretion rates do not have to be recalculated.

Accretion rates have been found to scale directly with  $H\alpha$  10% width (Natta et al. 2004). Therefore, accretion rates originally found using the Natta et al. (2004) scaling relation do not have to be recalculated; this encompasses all objects with  $H\alpha$  10% width within CASPAR.

# Appendix D Other Linear Fitting Techniques

It is well known that different linear regression procedures should be used, based on the data being considered. Significant work (Isobe et al. 1990; Feigelson & Babu 1992) has explored how these different algorithms affect astronomical data and

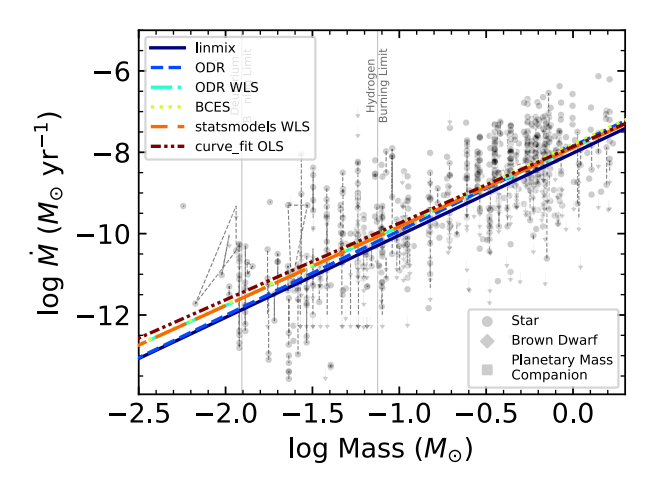


Figure 20. CASPAR accretion rate vs. mass with linear best fits from different linear regression algorithms. linmix takes into account all parameters, while the others take into account some parameters, as listed in Table 9.

Table 9
Linear Regression Algorithms

Fitting Algorithm	y Error	x Error	Upper Limits
linmix	X	x	Х
ODR	X	X	
ODR WLS	X		
BCES	X	X	
WLS	X		
OLS		•••	

Table 10 Linear Regression Results

Fitting Algorithm	$a(\pm \text{Error})$	$b(\pm { m Error})$
linmix	2.02(0.06)	-8.02(0.05)
scipy.ODR	2.08(0.05)	-7.85(0.04)
scipy.ODR WLS	1.94(0.06)	-7.89(0.05)
bces.BCES	1.97(0.06)	-7.80(0.05)
statsmodels.WLS	1.94(0.02)	-7.89(0.02)
curve_fit OLS	1.88(0.05)	-7.86(0.05)

results. As we explore the best linear fits for a variety of quantities in CASPAR, reliable fitting is necessary. linmix, a Bayesian linear regression routine (Kelly 2007), takes into account both x and y measurement errors as well as upper limits. In order to determine the extent to which these quantities affect the linear fits, we compare this fit to other fitting techniques that take into account a variety of these parameters. See Table 9. We use pythonto to derive the best fits for each technique:

- 1. orthogonal distance regression (ODR): scipy.ODR;
- 2. ordinary least squares bisector (BCES): bces;
- 3. weighted least squares (WLS): statsmodels. WLS; and
- 4. ordinary least squares (OLS): curve\_fit.

Figure 20 and Table 10 show the results. Algorithms that include x errors but do not properly take into account upper limits (ODR and BCES) still closely match linmix, while those that do not take into account error bars do not reproduce linmix. This is most prominent in the substellar regime, where the fits diverge significantly. Those without x errors consistently overestimate the intercept of the fit compared to those that take both x and y into account.

## Appendix E Separate Mass Population Fit Statistics

In Table 11, we compare the mean residual from each fit, the AIC, and the Akaike weights (w) for each fit. As our models have the same number of parameters, the AIC will inform the goodness of fit between the two models, with the minimum AIC corresponding to the preferred model. The Akaike weights are the relative likelihoods of the models; we assume that w > 0.95 indicates the statistically favored model.

*Stars.* We find similar AIC statistics for the best total fit to CASPAR and the star-only fit, with neither model preferentially preferred. This indicates that either fit can be used to model the data.

*BDs*. In the substellar regime, we find a small, though not statistically significant, difference in the residuals between the CASPAR total fit and the BD-only fit, with the mean decreasing from 0.25 to 0.23. However, from the AIC statistics and weights shown in Table 11, we can show that the BD-only fit is more significantly preferred than the CASPAR total best fit.

*PMCs*. The best fit clearly showed non-normal residuals for the PMCs. The PMC-only best fit is significantly preferred, with the mean of the residuals decreasing from 0.82 to 0.05.

**Table 11** Population Statistics

	Mean Residual	AIC	w	$R^2$
	(dex)			
Star fit	$0.12 \pm 0.82$	1892.66	0.99	0.35
Best fit	$0.17 \pm 0.82$	1905.76	0.001	0.34
BD fit	$0.25 \pm 1.09$	726.57	0.98	0.14
Best fit	$0.23 \pm 1.10$	735.46	0.02	0.11
Planet fit	$0.05 \pm 0.98$	110.73	0.99	0.002
Best fit	$0.82\pm0.99$	131.25	$4 \times 10^{-5}$	-0.71

**Note.** AIC: Akaike Information Criterion; w: Akaike weights; and  $R^2$ : coefficient of determination.

## Appendix F Separate Mass Population Fits for Individual SFRs

We examine substellar and stellar population best fits for individual SFRs in CASPAR, removing the need to fit for age. We select the  $\rho$  Ophiuchus ( $\sim$ 2 Myr), Taurus ( $\sim$ 2.5 Myr), and Upper Scorpius ( $\sim$ 10 Myr) regions, as they span a wide range

of ages. As shown in Figure 21, from just these three regions, we see a steepening slope ( $\alpha=0.52,\,1.61,\,4.66$ ) with age in the substellar regime, while the stellar regime appears to slightly flatten ( $\alpha=1.32,\,2.53,\,0.94$ ) for  $\rho$  Ophiuchus, Taurus, and Upper Scorpius, respectively, similar to the trends seen by Alcalá et al. (2017) and Manara et al. (2017a).

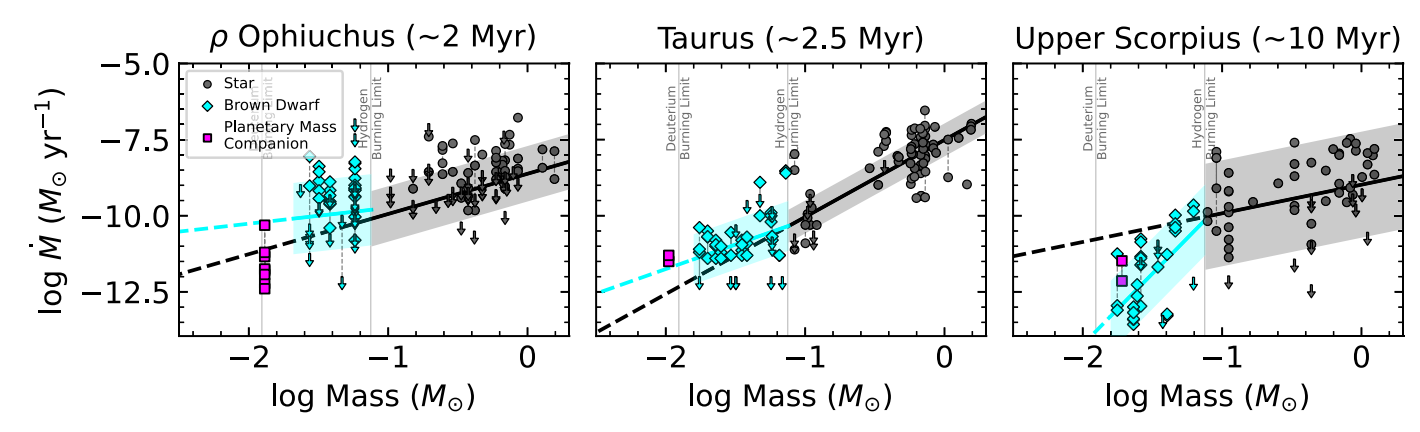


**Figure 21.** Accretion rate vs. mass for  $\rho$  Ophiuchus (left), Taurus (center), and Upper Scorpius (right). Colors and markers are as in Figure 15. The best linear fits (solid lines) and  $1\sigma$  scatters (bands) are shown for the star (black) and BD (cyan) populations. The dashed lines show the extrapolation into the planetary regime.

#### ORCID iDs

```
S. K. Betti https://orcid.org/0000-0002-8667-6428
K. B. Follette https://orcid.org/0000-0002-7821-0695
K. Ward-Duong https://orcid.org/0000-0002-4479-8291
A. E. Peck https://orcid.org/0000-0003-2461-6881
Y. Aoyama https://orcid.org/0000-0003-0568-9225
J. Bary https://orcid.org/0000-0001-8642-5867
S. Edwards https://orcid.org/0000-0002-3232-665X
G.-D. Marleau https://orcid.org/0000-0002-2919-7500
K. Mohamed https://orcid.org/0000-0001-9502-3448
C. Plunkett https://orcid.org/0000-0002-1144-6708
C. Robinson https://orcid.org/0000-0003-1639-510X
```

#### References

```
Alcala', J. M., Manara, C. F., France, K., et al. 2019, A&A, 629, A108
Alcalá, J. M., Gangi, M., Biazzo, K., et al. 2021, A&A, 652, A72
Alcalá, J. M., Majidi, F. Z., Desidera, S., et al. 2020, A&A, 635, L1
Alcalá, J. M., Manara, C. F., Natta, A., et al. 2017, A&A, 600, A20
Alcalá, J. M., Natta, A., Manara, C. F., et al. 2014, A&A, 561, A2
Alexander, R., Pascucci, I., Andrews, S., Armitage, P., & Cieza, L. 2014, in
   Protostars and Planets VI, ed. H. Beuther et al. (Tucson, AZ: Univ. Arizona
   Press), 475
Antoniucci, S., García López, R., Nisini, B., et al. 2014, A&A, 572, A62
Aoyama, Y., Ikoma, M., & Tanigawa, T. 2018, ApJ, 866, 84
Aoyama, Y., Marleau, G.-D., Mordasini, C., & Ikoma, M. 2020,
   arXiv:2011.0660
Armitage, P. J., Clarke, C. J., & Palla, F. 2003, MNRAS, 342, 1139
Astropy Collaboration, Price-Whelan, A. M., Sipőcz, B. M., et al. 2018, AJ,
   156, 123
Astropy Collaboration, Robitaille, T. P., Tollerud, E. J., et al. 2013, A&A,
   558, A33
Bailer-Jones, C. A. L., Rybizki, J., Fouesneau, M., Demleitner, M., &
   Andrae, R. 2021, AJ, 161, 147
Bailer-Jones, C. A. L., Rybizki, J., Fouesneau, M., Mantelet, G., & Andrae, R.
   2018, AJ, 156, 58
Baraffe, I., Elbakyan, V. G., Vorobyov, E. I., & Chabrier, G. 2017, A&A,
   597, A19
Baraffe, I., Homeier, D., Allard, F., & Chabrier, G. 2015, A&A, 577, A42
Bate, M. R., Bonnell, I. A., & Bromm, V. 2002, MNRAS, 332, L65
Bate, M. R., Bonnell, I. A., & Bromm, V. 2003, MNRAS, 339, 577
Bell, C. P. M., Mamajek, E. E., & Naylor, T. 2015, MNRAS, 454, 593
Bell, C. P. M., Naylor, T., Mayne, N. J., Jeffries, R. D., & Littlefair, S. P. 2013,
    INRAS, 434, 806
Betti, S., Follette, K., & Ward-Duong, K. 2023, Comprehensive Archive of
  Substellar and Planetary Accretion Rates, v1.0.1 Zenodo, doi: 10.5281/
   zenodo.10150171
Betti, S. K., Follette, K. B., Ward-Duong, K., et al. 2022, ApJL, 935, L18
Biazzo, K., Alcalá, J. M., Frasca, A., et al. 2014, A&A, 572, A84
Boss, A. P. 1997, Sci, 276, 1836
Bowler, B. P., Liu, M. C., Kraus, A. L., Mann, A. W., & Ireland, M. J. 2011,
Cai, K., Durisen, R. H., Michael, S., et al. 2006, ApJL, 636, L149
Calvet, N., & Gullbring, E. 1998, ApJ, 509, 802
Calvet, N., Muzerolle, J., Briceño, C., et al. 2004, AJ, 128, 1294
Cameron, A. G. W. 1978, M&P, 18, 5
Chabrier, G. 2005, in Astrophysics and Space Science Library, The Initial
   Mass Function 50 Years Later, ed. E. Corbelli, F. Palla, & H. Zinnecker,
   Vol. 327 (Dordrecht: Springer), 41
Choi, J., Dotter, A., Conroy, C., et al. 2016, ApJ, 823, 102
Claes, R. A. B., Manara, C. F., Garcia-Lopez, R., et al. 2022, A&A, 664, L7
Clarke, C. J., & Pringle, J. E. 2006, MNRAS, 370, L10
Close, L. M., Follette, K. B., Males, J. R., et al. 2014, ApJL, 781, L30
Comerón, F., Testi, L., & Natta, A. 2010, A&A, 522, A47
Costigan, G., Vink, J. S., Scholz, A., Ray, T., & Testi, L. 2014, MNRAS,
  440, 3444
DeSouza, A. L., & Basu, S. 2017, NewA, 51, 113
Doi, Y., Takita, S., Ootsubo, T., et al. 2015, PASJ, 67, 50
Dotter, A. 2016, ApJS, 222, 8
Dullemond, C. P., Natta, A., & Testi, L. 2006, ApJL, 645, L69
Dupree, A. K., Brickhouse, N. S., Cranmer, S. R., et al. 2014, ApJ, 789, 27
```

```
Ercolano, B., Mayr, D., Owen, J. E., Rosotti, G., & Manara, C. F. 2014,
   MNRAS, 439, 256
Eriksson, S. C., Asensio Torres, R., Janson, M., et al. 2020, A&A, 638, L6
Espaillat, C., Muzerolle, J., Hernández, J., et al. 2008, ApJL, 689, L145
Esplin, T. L., & Luhman, K. L. 2020, AJ, 159, 282
Esplin, T. L., & Luhman, K. L. 2022, AJ, 163, 64
Feiden, G. A. 2016, A&A, 593, A99
Feigelson, E. D., & Babu, G. J. 1992, ApJ, 397, 55
Fiorellino, E., Manara, C. F., Nisini, B., et al. 2021, A&A, 650, A43
Fischer, W., Edwards, S., Hillenbrand, L., & Kwan, J. 2011, ApJ, 730, 73
Gaia Collaboration, Brown, A. G. A., Vallenari, A., et al. 2018, A&A, 616, A1
Gaia Collaboration, Brown, A. G. A., Vallenari, A., et al. 2021, A&A, 649, A1
Gaia Collaboration, Prusti, T., de Bruijne, J. H. J., et al. 2016, A&A, 595, A1
Gagné, J., Mamajek, E. E., Malo, L., et al. 2018, ApJ, 856, 23
Galli, P. A. B., Bouy, H., Olivares, J., et al. 2020, A&A, 643, A148
Galli, P. A. B., Bouy, H., Olivares, J., et al. 2021, A&A, 646, A46
Gangi, M., Antoniucci, S., Biazzo, K., et al. 2022, A&A, 667, A124
Gatti, T., Natta, A., Randich, S., Testi, L., & Sacco, G. 2008, A&A, 481, 423
Gatti, T., Testi, L., Natta, A., Randich, S., & Muzerolle, J. 2006, A&A,
   460, 547
Ginsburg, A., Sipőcz, B. M., Brasseur, C. E., et al. 2019, AJ, 157, 98
Goodwin, S. P., Hubber, D. A., Moraux, E., & Whitworth, A. P. 2005, AN,
   326, 1040
Gullbring, E., Calvet, N., Muzerolle, J., & Hartmann, L. 2000, ApJ, 544, 927
Gullbring, E., Hartmann, L., Briceño, C., & Calvet, N. 1998, ApJ, 492, 323
Guzmán-Díaz, J., Mendigutía, I., Montesinos, B., et al. 2021, A&A, 650, A182
Haffert, S. Y., Bohn, A. J., de Boer, J., et al. 2019, NatAs, 3, 749
Harris, C. R., Millman, K. J., van der Walt, S. J., et al. 2020, Natur, 585,
Hartigan, P., Edwards, S., & Ghandour, L. 1995, ApJ, 452, 736
Hartmann, L. 1998, Accretion Processes in Star Formation (Cambridge:
   Cambridge Univ. Press)
Hartmann, L., Herczeg, G., & Calvet, N. 2016, ARA&A, 54, 135
Hashimoto, J., Aoyama, Y., Konishi, M., et al. 2020, AJ, 159, 222
Hawley, J. F., & Balbus, S. A. 1991, ApJ, 376, 223
Hayashi, C., Nakazawa, K., & Nakagawa, Y. 1985, in Protostars and Planets II,
   ed. D. C. Black & M. S. Matthews (Tucson, AZ: Univ. Arizona Press), 1100
Henderson, C. B., & Stassun, K. G. 2012, ApJ, 747, 51
Herczeg, G. J., Cruz, K. L., & Hillenbrand, L. A. 2009, ApJ, 696, 1589
Herczeg, G. J., & Hillenbrand, L. A. 2008, ApJ, 681, 594
Herczeg, G. J., & Hillenbrand, L. A. 2014, ApJ, 786, 97
Huang, Y., Beers, T. C., Wolf, C., et al. 2022, ApJ, 925, 164
Hubber, D. A., & Whitworth, A. P. 2005, A&A, 437, 113
Hunter, J. D. 2007, CSE, 9, 90
Ingleby, L., Calvet, N., Herczeg, G., et al. 2013, ApJ, 767, 112
Isobe, T., Feigelson, E. D., Akritas, M. G., & Babu, G. J. 1990, ApJ, 364,
   104
Jayawardhana, R., Mohanty, S., & Basri, G. 2003, ApJ, 592, 282
Johns-Krull, C. M., & Valenti, J. A. 2001, ApJ, 561, 1060
Johnson, B. M., & Gammie, C. F. 2003, ApJ, 597, 131
Kalari, V. M., & Vink, J. S. 2015, ApJ, 800, 113
Kalari, V. M., Vink, J. S., Drew, J. E., et al. 2015, MNRAS, 453, 1026
Kelly, B. C. 2007, ApJ, 665, 1489
Kirk, H., Johnstone, D., & Di Francesco, J. 2006, ApJ, 646, 1009
Kirkpatrick, J. D., Gelino, C. R., Faherty, J. K., et al. 2021, ApJS, 253, 7
Kounkel, M., Covey, K., Suárez, G., et al. 2018, AJ, 156, 84
Krolikowski, D. M., Kraus, A. L., & Rizzuto, A. C. 2021, AJ, 162, 110
Kuiper, G. P. 1951, PNAS, 37, 1
Lee, J., Song, I., & Murphy, S. 2020, MNRAS, 494, 62
Lesur, G., Flock, M., Ercolano, B., et al. 2023, in ASP Conf. Ser. 534,
   Protostars and Planets VII, ed. S. Inutsuka et al. (San Francisco, CA:
   ASP), 465
Li, M., & Xiao, L. 2016, ApJ, 820, 36
Lodato, G., Scardoni, C. E., Manara, C. F., & Testi, L. 2017, MNRAS,
   472, 4700
Luhman, K. L. 2020, AJ, 160, 186
Luhman, K. L. 2022, AJ, 163, 25
Luhman, K. L., Lada, C. J., Hartmann, L., et al. 2005, ApJL, 631, L69
Luhman, K. L., Stauffer, J. R., Muench, A. A., et al. 2003, ApJ, 593, 1093
Malo, L., Doyon, R., Feiden, G. A., et al. 2014, ApJ, 792, 37
Mamajek, E. E. 2009, in AIP Conf. Ser. 1158, Exoplanets and Disks: Their
   Formation and Diversity, ed. T. Usuda, M. Tamura, & M. Ishii (Melville,
Manara, C. F., Ansdell, M., Rosotti, G. P., et al. 2023, in ASP Conf. Ser. 534,
```

Protostars and Planets VII, ed. S. Inutsuka (San Francisco, CA: ASP), 539

```
Manara, C. F., Fedele, D., Herczeg, G. J., & Teixeira, P. S. 2016a, A&A,
   585, A136
Manara, C. F., Rosotti, G., Testi, L., et al. 2016b, A&A, 591, L3
Manara, C. F., Frasca, A., Alcalá, J. M., et al. 2017a, A&A, 605, A86
Manara, C. F., Testi, L., Herczeg, G. J., et al. 2017b, A&A, 604, A127
Manara, C. F., Frasca, A., Venuti, L., et al. 2021, A&A, 650, A196
Manara, C. F., Natta, A., Rosotti, G. P., et al. 2020, A&A, 639, A58
Manara, C. F., Testi, L., Natta, A., & Alcalá, J. M. 2015, A&A, 579, A66
Marleau, G.-D., & Aoyama, Y. 2022, RNAAS, 6, 262
Marleau, G. D., Aoyama, Y., Kuiper, R., et al. 2022, A&A, 657, A38
Martinez, R. A., & Kraus, A. L. 2019, AJ, 158, 134
Messina, S., Millward, M., Buccino, A., et al. 2017, A&A, 600, A83
Mohanty, S., Jayawardhana, R., & Basri, G. 2005, ApJ, 626, 498
Morton, T. D., 2015 isochrones: Stellar model grid package, Astrophysics
   Source Code Library, ascl:1503.010
Mulders, G. D., Pascucci, I., Manara, C. F., et al. 2017, ApJ, 847, 31
Muzerolle, J., Calvet, N., & Hartmann, L. 2001, ApJ, 550, 944
Muzerolle, J., Hillenbrand, L., Calvet, N., Briceño, C., & Hartmann, L. 2003,
    ApJ, 592, 266
Muzerolle, J., Luhman, K. L., Briceño, C., Hartmann, L., & Calvet, N. 2005,
   ApJ, 625, 906
Natta, A., Testi, L., Muzerolle, J., et al. 2004, A&A, 424, 603
Natta, A., Testi, L., & Randich, S. 2006, A&A, 452, 245
NguyenThanh, D., Phan-Bao, N., Murphy, S. J., & Bessell, M. S. 2020, A&A,
   634, A128
Ochsenbein, F., Bauer, P., & Marcout, J. 2000, A&AS, 143, 23
OrtizLeón, G. N., Loinard, L., Dzib, S. A., et al. 2018, ApJL, 869, L33
Pascucci, I., Cabrit, S., Edwards, S., et al. 2023, in ASP Conf. Ser. 534,
   Protostars and Planets VII, ed. S Inutsuka et al. (San Francisco, CA:
Paxton, B., Bildsten, L., Dotter, A., et al. 2011, ApJS, 192, 3
Paxton, B., Cantiello, M., Arras, P., et al. 2013, ApJS, 208, 4
Paxton, B., Marchant, P., Schwab, J., et al. 2015, ApJS, 220, 15
Pecaut, M. J., & Mamajek, E. E. 2016, MNRAS, 461, 794
Pecaut, M. J., Mamajek, E. E., & Bubar, E. J. 2012, ApJ, 746, 154
Petrus, S., Bonnefoy, M., Chauvin, G., et al. 2020, A&A, 633, A124
Pittman, C. V., Espaillat, C. C., Robinson, C. E., et al. 2022, AJ, 164, 201
Pollack, J. B., Hubickyj, O., Bodenheimer, P., et al. 1996, Icar, 124, 62
Pouilly, K., Bouvier, J., Alecian, E., et al. 2020, A&A, 642, A99
Prisinzano, L., Damiani, F., Kalari, V., et al. 2019, A&A, 623, A159
Rafikov, R. R. 2005, ApJL, 621, L69
Ratzenböck, S., Großschedl, J. E., Alves, J., et al. 2023, A&A, 678, A71
Rigliaco, E., Natta, A., Randich, S., Testi, L., & Biazzo, K. 2011, A&A,
   525, A47
Rigliaco, E., Natta, A., Testi, L., et al. 2012, A&A, 548, A56
Rilinger, A. M., & Espaillat, C. C. 2021, ApJ, 921, 182
```

Ringqvist, S. C., Viswanath, G., Aoyama, Y., et al. 2023, A&A, 669, L12

```
Rizzuto, A. C., Dupuy, T. J., Ireland, M. J., & Kraus, A. L. 2020, ApJ,
  889, 175
Rizzuto, A. C., Ireland, M. J., Dupuy, T. J., & Kraus, A. L. 2016, ApJ,
  817, 164
Rosotti, G. P., Clarke, C. J., Manara, C. F., & Facchini, S. 2017, MNRAS,
  468, 1631
Rugel, M., Fedele, D., & Herczeg, G. 2018, A&A, 609, A70
Safronov, V. S., & Zvjagina, E. V. 1969, Icar, 10, 109
Sallum, S., Follette, K. B., Eisner, J. A., et al. 2015, Natur, 527, 342
Salyk, C., Herczeg, G. J., Brown, J. M., et al. 2013, ApJ, 769, 21
Sanchis, E., Testi, L., Natta, A., et al. 2021, A&A, 649, A19
Santamaría-Miranda, A., Cáceres, C., Schreiber, M. R., et al. 2018, MNRAS,
  475, 2994
Schneider, A. C., Windsor, J., Cushing, M. C., Kirkpatrick, J. D., &
   Wright, E. L. 2016, ApJL, 822, L1
Sellek, A. D., Booth, R. A., & Clarke, C. J. 2020, MNRAS, 498, 2845
SiciliaAguilar, A., Hartmann, L., Calvet, N., et al. 2006, ApJ, 638, 897
Soderblom, D. R., Hillenbrand, L. A., Jeffries, R. D., Mamajek, E. E., &
  Naylor, T. 2014, in Protostars and Planets VI, ed. H. Beuther et al. (Tucson,
   AZ: Univ. Arizona Press), 219
Stamatellos, D., & Herczeg, G. J. 2015, MNRAS, 449, 3432
Strom, K. M., Strom, S. E., Edwards, S., Cabrit, S., & Skrutskie, M. F. 1989,
  AJ, 97, 1451
Takita, S., Doi, Y., Ootsubo, T., et al. 2015, PASJ, 67, 51
Testi, L., Natta, A., Scholz, A., et al. 2016, A&A, 593, A111
Thanathibodee, T., Calvet, N., Bae, J., Muzerolle, J., & Hernández, R. F. 2019,
   ApJ, 885, 94
Valenti, J. A., Basri, G., & Johns, C. M. 1993, AJ, 106, 2024
van Leeuwen, F. 2007, A&A, 474, 653
Venuti, L., Bouvier, J., Flaccomio, E., et al. 2014, A&A, 570, A82
Venuti, L., Stelzer, B., Alcalá, J. M., et al. 2019, A&A, 632, A46
Vioque, M., Oudmaijer, R. D., Wichittanakom, C., et al. 2022, ApJ, 930, 39
Virtanen, P., Gommers, R., Oliphant, T. E., et al. 2020, NatMe, 17, 261
Vorobyov, E. I., & Basu, S. 2008, ApJL, 676, L139
Vorobyov, E. I., & Basu, S. 2009, ApJ, 703, 922
Wagner, K., Follete, K. B., Close, L. M., et al. 2018, ApJL, 863, L8
Ward-Duong, K., Patience, J., Bulger, J., et al. 2018, AJ, 155, 54
Wenger, M., Ochsenbein, F., Egret, D., et al. 2000, A&AS, 143, 9
White, R. J., & Basri, G. 2003, ApJ, 582, 1109
Wright, N. J., Jeffries, R. D., Jackson, R. J., et al. 2019, MNRAS, 486, 2477
Wu, Y.-L., Close, L. M., Males, J. R., et al. 2015, ApJ, 801, 4
Wu, Y.-L., Sheehan, P. D., Males, J. R., et al. 2017, ApJ, 836, 223
Zagaria, F., Clarke, C. J., Rosotti, G. P., & Manara, C. F. 2022, MNRAS,
Zhou, Y., Herczeg, G. J., Kraus, A. L., Metchev, S., & Cruz, K. L. 2014, ApJL,
  783, L17
Zuckerman, B. 2019, ApJ, 870, 27
```